Journal of the European Ceramic Society 45 (2025) 117230

Contents lists available at ScienceDirect

Journal of the European Ceramic Society

journal homepage: www.elsevier.com/locate/jeurceramsoc

Sintering mechanisms, phase transformations and microstructure of porcelain stoneware containing thermally inertized man-made vitreous fibres

Sonia Conte [a,*], Riccardo Fantini [b], Rossella Arletti [b], Chiara Molinari [a], Michele Dondi [a], Chiara Zanelli [a], Alessandro F. Gualtieri [b]

[a] CNR-ISSMC, National Research Council, Institute of Science, Technology and Sustainability for Ceramics, Via Granarolo 64, Faenza 48018, Italy
[b] Department of Chemical and Geological Science, University of Modena and Reggio Emilia, Via Giuseppe Campi 103, Modena 41125, Italy

ARTICLE INFO

Keywords:
Porcelain stoneware
Inertized vitreous fibres
Sintering mechanisms
Phase composition
Microstructure

ABSTRACT

The waste incorporation into porcelain stoneware is a key strategy for enhancing sustainability in ceramic production. To achieve a satisfactory finished product, a crucial aspect to be investigated is the effect that a waste can induce on the tile sintering behaviour, which, in turn, determines its final technological properties. This study investigates the effect of a glass deriving from the thermal inertization of man-made vitreous fibres on the sintering of porcelain stoneware tiles, obtained by pressing and fast firing. Results indicated that it is easier to incorporate into porcelain stoneware than other peralkaline glasses, due to its tendency to crystallize in the early stage of the densification process, limiting the interaction with the ceramic matrix and allowing the achievement of a good densification. Otherwise, the microstructure of the fired tiles in overfiring conditions is influenced, since the loss of bulk viscosity and likely the Fe^{3+} reduction led to bloating phenomena.

1. Introduction

Silicate ceramics are good waste acceptors, since they are made up of a heterogeneous mixture of minerals, which is intrinsically prone to accommodating extraneous components. The introduction of waste into ceramic bodies is tolerated as far as its technological behaviour resembles those of conventional raw materials. This implies that variations in the production process and of the properties of semi-finished and finished products must be manageable with the ceramic facilities [1–5]. Porcelain stoneware, being one of the prevailing typologies of traditional ceramic tiles globally produced [6,7], is the main target of waste recycling, accounting for more R&D studies than any other ceramic tile type. Since light-coloured bodies, such as porcelain stoneware, are obtained by complex batches, the main technological role of the waste must be predicted prior to introduce it in replacement of a given type of raw material. Literature data indicate that the most common substitution in these bodies is waste in replacement of flux (66 % of the 120 analysed papers in Zanelli ad co-workers [4]), and less frequently of plastic component (22 %) or filler (12 %). Many kinds of waste, such as those from mining, quarrying and treatment of minerals, from thermal processes, from construction, demolition, and dredging, from inorganic chemical processes, from the production of ceramics, glasses, and refractories, and so on, were tested at different technology readiness levels (TRLs). Among them, Soda-Lime-Silica (SLS) glass, residues of the tile-making process, and waste from minerals extraction, showed the higher TRL (9), being already employed as technological solution industrialized and put on the market [4]. Indeed, the use of waste glasses in the ceramic tile production has been extensively investigated in the last decades, for their fluxing power able to lower the firing temperature [8]. The technological behaviour of porcelain stoneware bodies containing SLS glass has been thoroughly investigated, especially for as concerns the firing stage [5,9–23]. In depth examination of sintering behaviour in terms of kinetics, phase transformations and microstructure was also carried out [24–26]. These studies improved the understanding of the SLS glass effect beyond its fluxing role, disclosing the evolution of melt properties with firing and the sintering mechanisms. The same degree of investigation is not found for other types of glass introduced into porcelain stoneware batches. Technological data are available, although much less than SLS, for glasses from Waste Electrical and Electronic Equipment (WEEE): PC-TV screen [14,27,28], PC-TV cathodic tube

* Corresponding author.
E-mail address: sonia.conte@issmc.cnr.it (S. Conte).

https://doi.org/10.1016/j.jeurceramsoc.2025.117230
Received 29 November 2024; Received in revised form 9 January 2025; Accepted 19 January 2025
Available online 21 January 2025

(CRT) [11,14,27]; other post-consumer glasses (such as thin-film transistor liquid-crystal display TFT- LCD [29], vial [30]); glasses from waste melting (municipal solid waste incinerator fly ashes by the application of thermal plasma melting [31], vitrified wastes, such as feldspar mining residues and lime from fume abatement system of the glass industry, admixed with SLS or PC-TV glass [32,33]). On the other hand, the effect that these kinds of glass can induce on the sintering behaviour of porcelain stoneware bodies has been seldom investigated [25]. Actually, all of them are amorphous materials (or present a negligible crystalline component), and can be basically distinguished on their chemical composition, which is usually far from that of conventional fluxes (*i.e.,* feldspar). The introduction of a glass with a very different composition, compared to feldspathic fluxes, can induce effects on the vitrification, mullitization and even recrystallization paths, as well as on the physical properties of the melt, such as shear viscosity and surface tension, which govern the sintering. This aspect turns to be crucial and cannot be generalized in the case of glasses derived from waste melting, since their chemical composition strongly depends on the types of residues and additives involved in the vitrification treatment, so their behaviour has to be evaluated case by case.

In this work, the effect of a glass deriving from the thermal inertization of man-made vitreous fibres (MMVF) – with a composition lower in silica and higher in Ca-Mg-Fe with respect to a feldspar – on the sintering of porcelain stoneware bodies is addressed. The inertization process of the fibres into massive glass and the technological feasibility of incorporating this glass into porcelain stoneware batches have been already assessed in a previous study [34]. Here the goal is to shed light on sintering mechanisms, particularly kinetics and efficiency of densification, phase transformations and microstructure of porcelain stoneware containing this inertized product.

2. Experimental

The four different batches analysed here were previously produced to assess the technological feasibility of the use of inertized man-made vitreous fibres, named Re.Wo. (*Recycled wool*), for porcelain stoneware production [34]. The batches considered are a benchmark, named V0, representing a classical industrial formulation for porcelain stoneware, and three batches with increasing additions of Re.Wo. in substitution of feldspars: 3 wt% (V3), 6 wt% (V6) and 9 wt% (V9). Formulations of the batches and their chemical composition (wt%) are reported in Table S1, supplementary materials. These batches underwent the simulation of the industrial tile-making process at the laboratory scale. The raw materials were ball milled in a porcelain jar using dense alumina grinding media, 40 wt% water (by weight of the slip) and 0.3 wt% deflocculant (sodium tripolyphosphate) by weight of dry batch, for 15 min. The slips were oven dried, de-agglomerated using a hammer mill with grid of 500 μm and manually granulated exploiting a sieve 2 mm with moisture ~ 8 wt% as in use in the industrial practice. Powders were compacted with a hydraulic press at 40 MPa into 110 × 55 × 5 mm tiles and then dried in oven at 105 °C overnight. The tiles were fired at different maximum temperature (T_{max}) based on their thermal behaviour: the benchmark V0 was fired at T_{max} = 1180, 1200, 1220 and 1240 °C, while batches containing Re.Wo. were fired at T_{max} = 1160, 1180, 1200 e 1220 °C. The results of the laboratory-scale simulation demonstrated that the introduction of Re.Wo., within certain limits, retains the properties required for the semi-finished and finished products. This despite the relatively high amount of iron oxide (up to 1.2 wt%), beyond the values typical for porcelain stoneware [34].

In the present work, the sintering behaviour of the four batches was evaluated by hot stage microscopy, using an optical thermo-dilatometer (TA, ODP868, Germany) which registered the size variation of a 5 × 5 × 5 mm chip cut from the dry samples, determined by the pixel count during a thermal cycle. The tests were run under isothermal conditions at different maximum temperatures, from 1100 up to 1220 °C, with a gradient of 80 °C x min^{-1} and dwell time of 30 min. Results were expressed in terms of both areal and linear firing shrinkage as a function of time [35,36]. Different stages of the sintering process were identified with reference to the densification curve, as described in Figure S1, supplementary materials. Isothermal sintering rates were calculated from early, linear and decreasing shrinkage (derived from specimen height variation) by dwell time at the various maximum temperatures. These *in-situ* tests also allowed the determination of the kinetics in the de-sintering stage, *i.e.,* the stage consisting in an inversion of the sintering process that may occur once the maximum density is reached, leading to a more or less accentuated expansion of the ceramic body.

Other properties were calculated as follows: relative density – of both unfired and fired bodies –with respect to specific weight by He-pycnometry (ASTM C329); closed porosity = total – open, total porosity calculated by He-pycnometry; efficiency of densification (*i.e.*, the density gained during the firing) as (relative density after firing – unfired relative density) * 100.

Quantitative phase analyses (QPA) of all the fired tiles were obtained from Rietveld refinement. X-Ray powder diffraction patterns were collected using a θ–θ Bragg-Brentano PANalytical 'XPert Pro Diffractometer equipped with a Cu Kα radiation (λ 1.5418 Å) tube operating at 40 kV and 40 mA and with a real time multiple strip (RTMS) detector. The samples were ground using an agate mortar and the powder was mixed with 10 wt% of corundum (α-Al_2O_3) NIST 676a as an internal standard. Data were collected in the angular range 3–110°2θ, using a step scan of 0.0167°2θ and a counting rate of 12 s/step. A 0.5° divergence slit was used together with 0.04 rad Soller slits. The XRPD patterns were analysed using the X-Pert High Score Plus suite [37]. To obtain quantitative phase analyses the Rietveld method was used [38,39], and the data were fitted using the Profex version 5.3.0 software [40]. The crystal structures employed for the Rietveld refinements and other details are reported in Table S2, while selected XRPD patterns are shown in Figure S2 (both in supplementary materials). A qualitative XRPD analysis was also performed on the V9 sample (fired at 1160 °C) after etching the powder in HF 15 %. This data collection was performed in the 27–32 °2θ, with step size of 0.0167°2θ and a counting rate of 600 s/step.

The chemical composition of the vitreous phase was estimated based on the quantitative chemical and phase composition of fired body by subtracting the chemical contribution of each crystalline phase, considering its stoichiometric formula, from the bulk chemistry (the resulting values were normalized to 100 %). The physical properties of the non-crystalline phase at high temperature were estimated by predictive models based on its chemical composition. The shear viscosity was calculated based on the Giordano-Russell-Dingwell model [41], and the gas–liquid surface tension was estimated interpolating the data obtained by Appen's [42] and Dietzel's [43] methods. The melt timescale was calculated based on Vasseur et al. [44], as (melt viscosity × mean particle size) / surface tension. Moreover, the effective viscosity of the body (η_{eff}) was calculated as the product of the shear viscosity of the melt (η_{melt}) by the relative viscosity (η_{rel}), *i.e.,* $\eta_{eff} = \eta_{rel} \times \eta_{melt}$ [25,35]. The relative viscosity was estimated by the relation: $\eta_{rel} = [1-(\phi/\phi_m)]^{-B\phi m}$, where ϕ is the solid load, ϕ_m is the critical fraction (set to 0.72) and B is the Einstein constant (*i.e.,* $B = 2.5$) [45].

The microstructural evolution of the fired ceramic batches and the analysis of phase assemblages and morphology were studied on polished samples embedded in epoxy resins. To have more detailed information, the samples' surface was etched for 4 min with a 15 % HF solution, washed ultrasonically with distilled water and dried. In both cases the samples were coated with carbon film to prevent charging under the electron beam. The analyses were carried out exploiting a scanning electron microscope (SEM) (JSM-6010 LA InTouchScope, JEOL, USA) equipped with a silicon-drift energy dispersive X-ray spectroscopy (EDS) detector (energy resolution: 133 eV or better) and FEG-SEM FEI Nova Nano-SEM 450, equipped with a Bruker XFlash-5010 EDS detector (energy resolution: 126 eV). EDS analyses of specific areas of interest, conducted to gain better understanding of element diffusion, were

performed exploiting the Phi- Rho-Z method and several analytical points and chemical maps per sample were collected. Images were obtained using both backscattered and secondary electron detectors.

The same HF-etched specimens employed for SEM analyses, without carbon coating, were also used for Micro-Raman spectroscopy. The experiment was performed using a confocal Horiba LabRAM HR Evolution (Horiba Jobin Yvon, Edison, NJ, United States) microspectrometer in backscattering geometry, with notch filters to eliminate the exciter, detector CCD front illuminated open electrode multipin phased, with 1024 × 256 × 16 pixels, cooled by a Peltier system. The employed source was a Nd-YAG laser of 532 nm. Spectra were collected at 50x magnification (1 μm-size spot, maximum power at the sample of 100 mW) with 30 s exposure time for three accumulations. LabSpec6 was used for the spectra elaboration.

3. Results and discussion

3.1. Sintering mechanisms and kinetics

The firing behaviour of the ceramic bodies was previously studied by *ex-situ* tests, firing the powder compacts in an electric roller kiln at different T_{max} (1160, 1180, 1200, 1220 and 1240 °C), to follow the technological properties of the tiles over a wide thermal range: from an incomplete sintering to overfiring conditions [34]. The maximum densification temperature was 1220 °C for V0 and V3 and 1200 °C for V6 and V9. In this work, the sintering mechanisms of the batches were investigated by *in-situ* experiments through hot stage microscopy (HSM) under isothermal conditions, with runs at different temperatures (1100, 1150, 1200 and 1220 °C). The main parameters resulting from HSM tests are reported in Table 1.

The temperatures at which the densification starts are quite variable, even so, the average of the four isothermal runs of each sample shows a linear decrease with the increase of Re.Wo. concentration, from 1053 °C of V0 down to 1017 °C of V9. The behaviour of the four bodies just slightly differs as extent of sintering stages (Fig. 1). There is a modest increase in the extent of the constant rate phase and a limited reduction of the decreasing stage as the Re.Wo. increases. Actually, the last stage of the sintering is predominant in all the bodies. This feature, with 45–60 % of the entire shrinkage occurring during the decreasing stage, is in contrast with what previously observed for porcelain stoneware bodies containing glassy waste, where the introduction of an increasing amount of glass induced a significant shortening of the final stage in favour of the non-isothermal early stage. This imbalance in the extent of the stages provoked a lower efficiency of densification in the bodies containing glassy waste with respect to the benchmark [25,26].

This phenomenon is not observed adding Re.Wo. glass to the ceramic batch: being the last stage of sintering well represented, the densification degree is quite comparable for all the samples, as reported by the sintering curves collected at the temperatures of maximum densification for each body, *i.e.*, 1220 °C for V0 and V3, 1200 °C for V6 and V9 (Fig. 2A). The sintering proceeds with similar behaviour for V0-V3-V6, which reached their maximum linear shrinkage (5.5–6.7 %) followed by a good stability during the 30 min at dwell temperature. An incipient bloating can be perceived for V3 and V6, occurring after a stable plateau, extended over 8–9 min (Table 1). On the other hand, the shrinkage observed for batch V9 keeps going on during the dwell time, reaching values even higher than the benchmark at the end of the run (6.9 % of linear shrinkage, after 30 min, Fig. 2B).

In order to verify the effective densification efficiency of the ceramic products at the end of firing, we have to take into account *ex-situ* experiments, which simulate the industrial firing cycle (40 °C·min^{-1}, 5 min of dwell time) and evaluate it in terms of density gain during firing. Data reported in Table 2 indicate a very similar efficiency of densification for V0 and V3 at T_{md}, ~17 %, while it slightly decreases with the increasing of Re.Wo. in the batches (~16 % in V6-V9 at T_{md}).

The drop of the densification efficiency is more evident when comparing all the batches at the same temperature of 1220 °C. The important loss of bulk density of V6 and V9 is due to the increase of closed porosity, up to values well above those observed for well densified porcelain stoneware [26,46]. In this sense, the HSM tests confirmed the overfiring conditions with the occurrence of bloating after a short plateau of stability (less than 1 min) for both the batches at 1220 °C (Table 1).

HSM isothermal runs also allowed to determine the sintering kinetics for each step of sintering (Table 1, Fig. 3). The sintering rates vary depending on the stage considered: they are slow in the early stage, accelerate during the constant rate phase (with a significant increase as temperature rises), and then slow down again in the final stage. Differences in kinetics emerged between the four samples at the highest temperature, in which the Re.Wo.-bearing bodies exhibit a faster sintering rate than the benchmark, especially in the decreasing rate stage.

Table 1
Firing behaviour of ceramic batches in the HSM tests. The densification stage's extent along with the rate are reported for the early, constant and decreasing stages along with the total sintering rate, the plateau of stability and the bloating rate (when observed). The value reported are referred to the range and formulas described in Figure S1.

	Firing T	Start of densification	Early stage extent	Constant stage extent	Decreasing stage extent	Early stage rate	Constant stage rate	Decreasing stage rate	Sintering rate (total)	Plateau of stability[1]	Bloating rate
Unit	°C	°C	%vol	%vol	%vol	%/min	%/min	%/min	%/min	s	%/min
V0	1100	1049	21 %	28 %	52 %	0.76	0.21	0.03	0.06	-	-
	1150	1077	7 %	32 %	61 %	0.58	0.44	0.08	0.12	-	-
	1200	1032	16 %	32 %	52 %	0.56	1.08	0.14	0.23	-	-
	1220 *	1053	20 %	25 %	54 %	0.85	1.93	0.19	0.31	-	-
V3	1100	1042	18 %	37 %	46 %	0.57	0.15	0.03	0.06	-	-
	1150	1000	17 %	30 %	53 %	0.45	0.43	0.07	0.13	-	-
	1200	1053	17 %	35 %	48 %	0.62	1.32	0.14	0.25	-	-
	1220 *	1022	17 %	33 %	50 %	0.55	1.81	0.20	0.36	513	0.02
V6	1100	1016	27 %	32 %	40 %	0.50	0.21	0.03	0.06	-	-
	1150	1028	16 %	31 %	53 %	0.31	0.45	0.07	0.12	-	-
	1200 *	1002	20 %	35 %	45 %	0.70	1.49	0.20	0.37	503	0.05
	1220	1031	25 %	35 %	40 %	0.65	1.45	0.22	0.42	34	0.09
V9	1100	1022	27 %	28 %	46 %	0.41	0.25	0.03	0.06	-	-
	1150	1011	16 %	31 %	53 %	0.39	0.44	0.07	0.12	-	-
	1200 *	991	13 %	28 %	58 %	0.45	1.28	0.17	0.25	-	-
	1220	1042	16 %	43 %	41 %	0.51	1.41	0.22	0.39	50	0.07

[1] = time between the achievement of maximum densification and the start of bloating; * = maximum densification temperature.

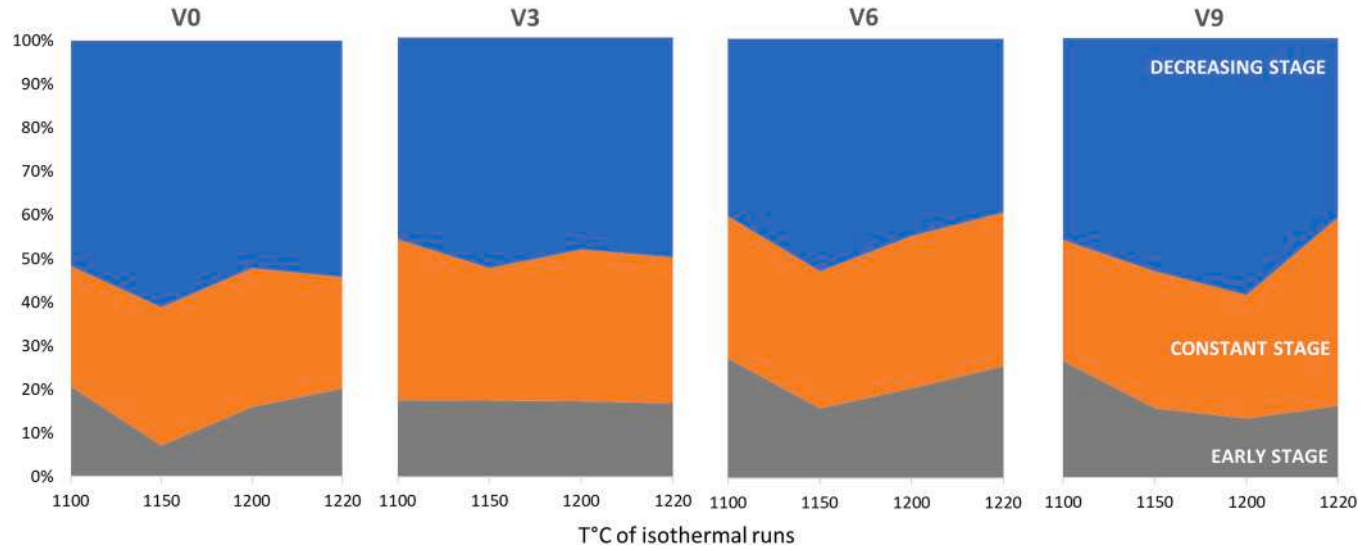

Fig. 1. Extent of densification in the early, constant and decreasing stages *vs*. temperature (°C) of isothermal runs, as reported in Table 1.

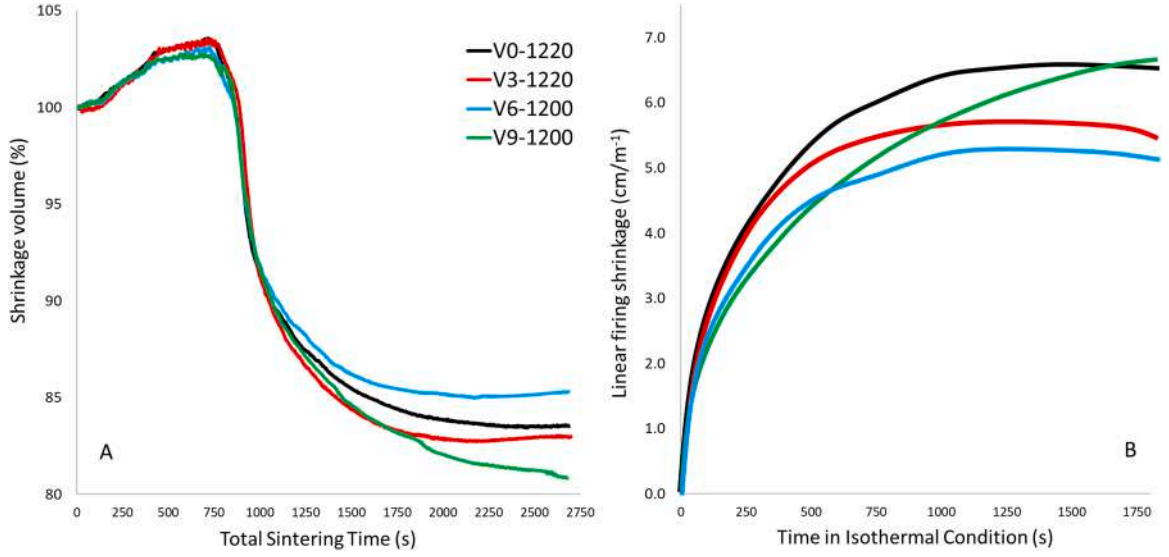

Fig. 2. Firing behaviour by HSM data (*in-situ* experiments) at the specific greisification temperatures: (A) volume shrinkage *vs*. total sintering time; (B) linear firing shrinkage *vs*. time from the achievement of T_{md}.

Table 2
Firing behaviour of ceramic batches, elaboration of *ex-situ* tests and pycnometry data.

	Firing T °C	Bulk density (unfired)[1] g/cm^3	Real density (unfired) g/cm^3	Relative density (unfired)[2] adim.	Bulk density (fired)[1] g/cm^3	Real density (fired) g/cm^3	Relative density (fired)[2] adim.	Closed porosity % volume	Efficiency of densification (density gain during firing) %
V0	1200	2.016 (5)	2.617 (2)	0.770	2.344 (3)	2.524 (1)	0.929	1.91	15.9
	T_{md}				2.365 (2)	2.501 (1)	0.946	4.01	17.6
	1220								
V3	1200	2.001 (4)	2.640 (1)	0.758	2.362 (1)	2.524 (1)	0.936	3.72	17.8
	T_{md}				2.333 (4)	2.512(1)	0.929	6.53	17.1
	1220								
V6	T_{md}	2.015 (5)	2.628 (1)	0.767	2.357 (1)	2.538 (1)	0.929	6.04	16.2
	1200								
	1220				2.278 (1)	2.524 (1)	0.903	9.41	13.6
V9	T_{md}	2.016 (4)	2.639 (2)	0.764	2.345 (3)	2.544 (1)	0.922	7.20	15.8
	1200								
	1220				2.198 (3)	2.518 (1)	0.873	12.37	10.9

[1=] data from Arletti et al. [34]; [2=] Bulk density/Real density.

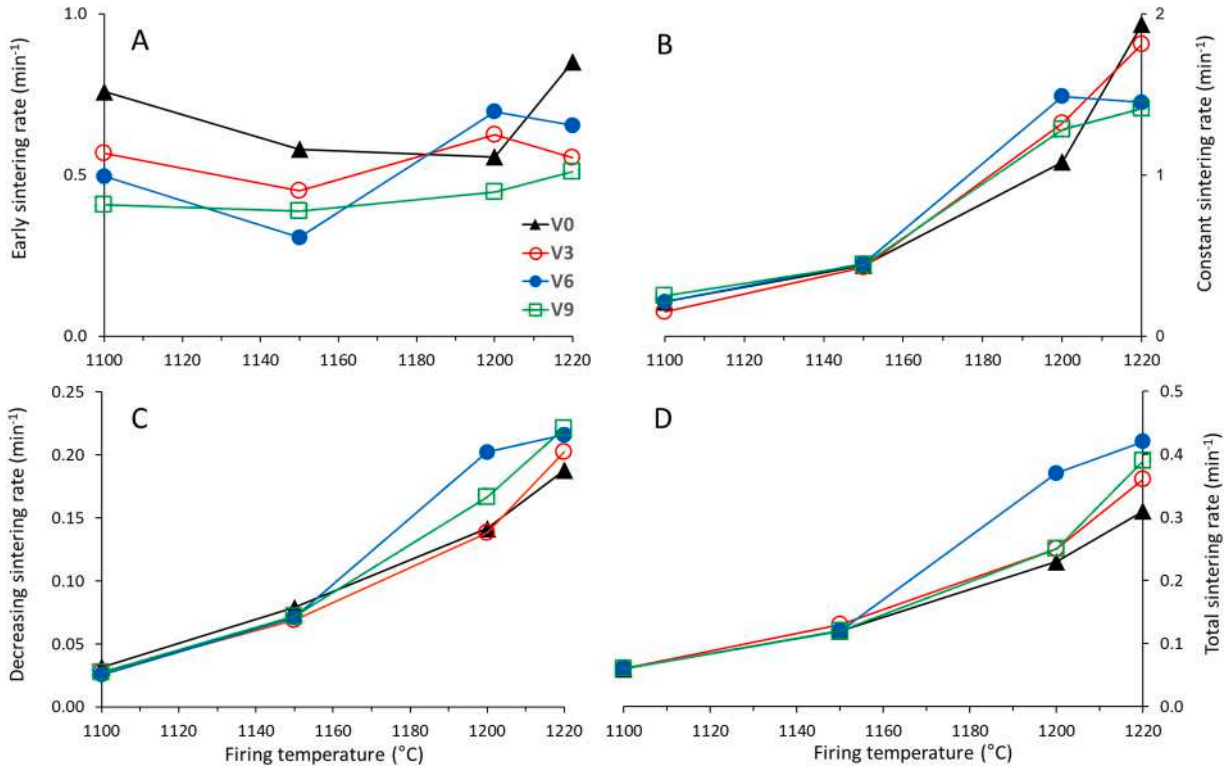

Fig. 3. Sintering kinetics in A) early stage, B) constant stage; C) decreasing stage; D) the whole sintering process. Experimental error is within the symbol size.

3.2. Phase evolution

The phase evolution of the ceramic batches with firing temperature is summarised in Fig. 4 and Table S2, supplementary materials.

Quartz partially melted during firing [47–50], with a clearly different stability as a function of the Re.Wo. content. There is a relationship between the amounts of waste glass and residual quartz: the greater is the Re.Wo. addition, the lower is the quantity of quartz present in the fired bodies. Indeed, at 1220 °C, the residual fraction of quartz, expressed as percentage of the amount in the unfired body, decreases to 93 % for V0 and to 70 % for V9, with V3 and V6 representing intermediate values. This effect is due to the peralkaline composition of Re.Wo., richer in Ca, Mg, and Na than in Al (molar base). These chemical features induce a shift in the composition of the ceramic batch, from frankly peraluminous (benchmark) towards the peralkaline field, which enhances the stability of feldspars at the expense of mullite formation and quartz persistence (Figure S3, supplementary materials), as observed in the literature [25,26,46,51–53]. Moreover, there is an increase of the quartz dissolution rate for the benchmark between 1220 and 1240 °C, with a drop of ~15 %, which induces a significant growth in the amorphous phase, thus vitrification degree.

Plagioclase progressively melted during firing in all the batches, as expected [26,35,54]. All trends run linearly with temperature and proportionally to the Re.Wo. contents. Indeed, the Re.Wo.-bearing bodies show at the end of firing at T_{md} a high content of plagioclase (9–12 wt% for V6-V9, respectively), despite their initial content was lower with respect to V0 (being the waste glass introduced in substitution of feldspar). As mentioned before, this could be expected, considering the chemical composition of the bodies with Re.Wo., based on previous research about porcelain stoneware containing glassy waste [25,26], strong fluxes [46], as well as biomass bottom ash [51].

Mullite exhibits diverse trends in the four bodies. In V0, its amount increased up to 1220 °C, reaching a mullitization index (*i.e.,* the maximum quantity of mullite that can be formed by stoichiometric reaction from kaolinite (55 %) and illite (34 %) of the batch) of 75 %, then slightly decreased after firing at 1240 °C. The percentage of mullite was rather constant in V3, while in V6 and particularly in V9 its amount decreased regularly as the temperature increased, with a drop of the mullitization index down to 45 %, differently from what expected for a classical porcelain stoneware [55]. It is known from the literature that the efficiency by which Al_2O_3 contained in kaolinite and illite is converted into mullite (and this latter is preserved at the end of firing) does not depend only on clay minerals, but also on the total amount of alumina in the batch and its ratio with the alkalis [35,53]. In this work, indeed, the introduction of Re.Wo. shifts the chemistry of the ceramic body toward the peralkaline field (Figure S3, supplementary materials). As mentioned above, this tends to decrease the mullite stability. It should also be taken into account that the addition of other compounds to ceramic batches, such as CaO-rich ones, may induce the formation of different phases by reacting with Al_2O_3 sources, such as anorthite, thus competing with mullite [30,32,56,57]. Despite the quite high CaO content of the Re.Wo. (19.9 wt%, Table S3, supplementary materials), no anorthite was identified during XRPD or SEM analyses, while small amount of augite was highlighted as discussed in Section 3.3.1.

Magnetite was detected only in the batches containing waste glass and its amount, even if very low and near to the quantification limit of the method (generally 0.1–0.5 wt%, for details see Table S2, supplementary materials), is proportional to the Re.Wo. additions in the starting bodies. Magnetite content tends to decrease with the temperature: the dissolution rate appears to be quite slow and regular for V3, while V6 and V9 are characterized by a faster dissolution rate at the highest temperatures, with a loss of 30–50 % of magnetite after firing at 1200 and 1220 °C.

The amorphous phase grew with the firing temperature, reflecting the dissolution degree and rate of the different phases. A quite linear growth is observed for V3-V6-V9, corresponding to almost constant dissolution rates of quartz and plagioclase, while the trend is nonlinear for V0, dictated by a higher dissolution rate of quartz between 1220 and 1240 °C. The degree of vitrification at T_{md} are comparable for all the bodies, with values between 63 and 66 wt%, falling in the typical range

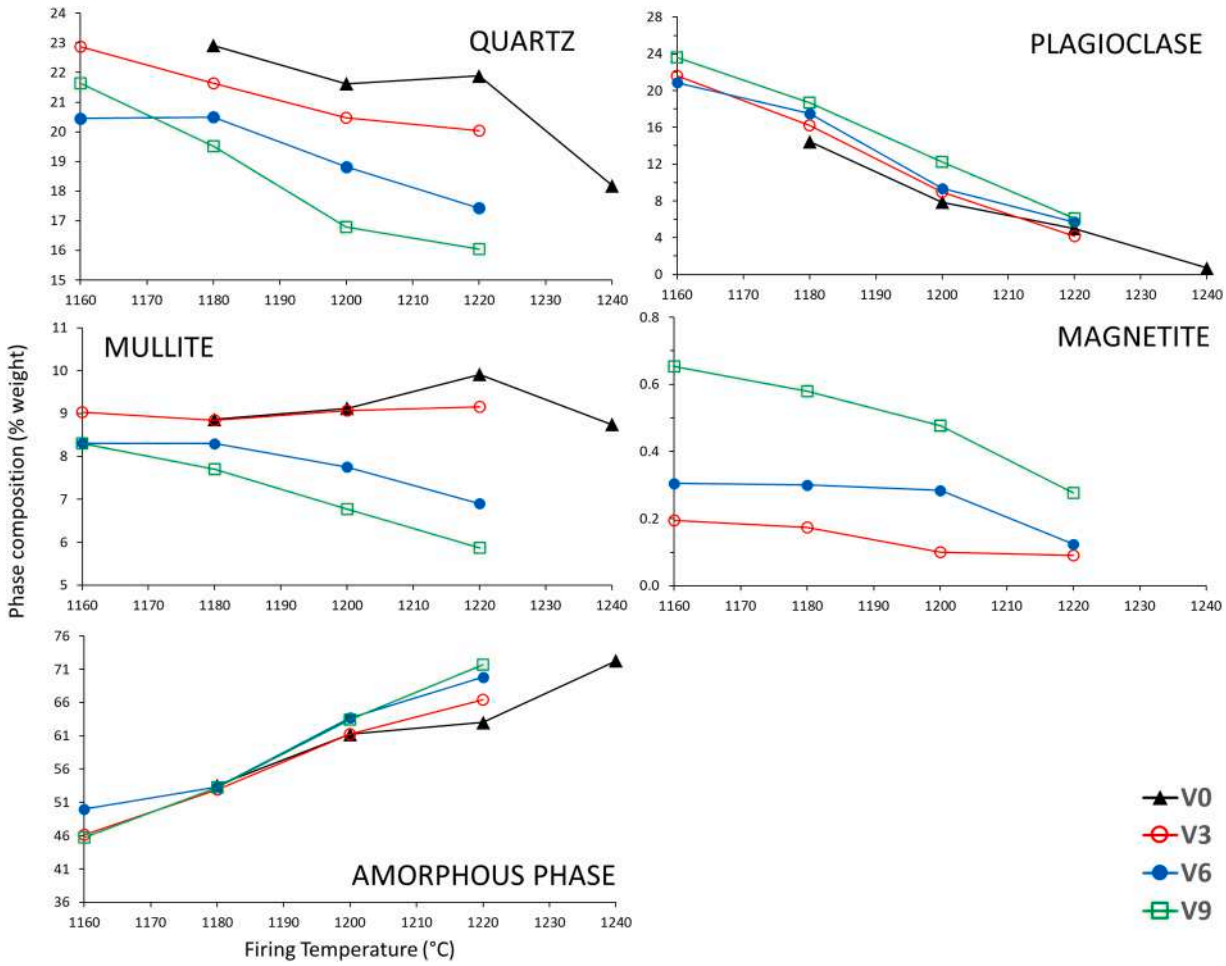

Fig. 4. Phase composition (% weight) of porcelain stoneware bodies as a function of firing temperature (°C). Experimental error is within the symbol size.

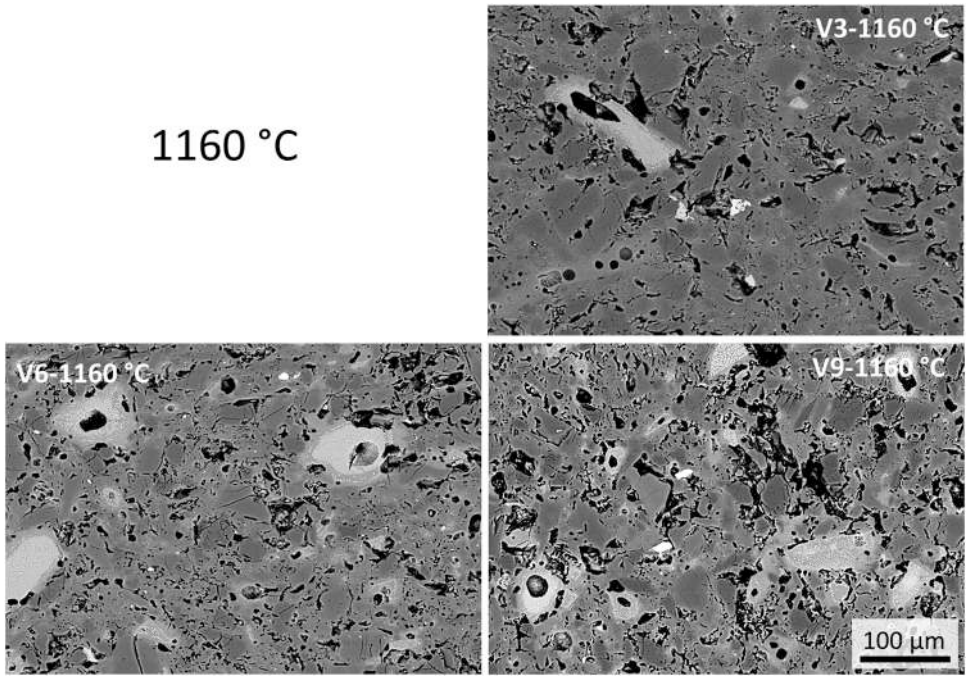

Fig. 5. Backscattering scanning electron microscope image of sample V3, V9 and V9 fired at 1160 °C.

of porcelain stoneware [35,50].

3.3. Microstructure

3.3.1. Firing at 1160 °C (V3-V6-V9)

At the lowest temperature considered (Fig. 5), all samples exhibit the microstructure of partially sintered bodies, with abundant open and interconnected porosity. This is particularly true for the V9 batch, which still shows crystals with sharp edges, embodied in the vitreous matrix stemming from the melting of feldspars. Indeed, as it can be seen from the graphs of phase evolution (Fig. 4), at this temperature the amorphous phase is ~46 wt% for V9 and higher in the other batches (up to 50 wt%). However, the peculiar feature of these microstructures is the presence of highly backscattering zones, characterized by a coarse pore inside, in amount increasing with increasing Re.Wo. addition.

A detailed investigation – with the analysis of elemental distribution maps – allowed to identify in these zones the occurrence of two kinds of crystals rich in iron, calcium and magnesium. Specifically, smaller sized and iron-rich crystals, located at the edge of the scattering zone, and elongated crystals enriched in Fe-Ca-Mg, in the middle, around the cavity (Fig. 6). The iron-rich crystals can be easily attributed to magnetite, detected by XRD and already discussed in paragraph 3.2. On the contrary, the Fe-Ca-Mg phase was not detected by XRPD analyses, being below the detection limit. Since magnetite was found only in bodies containing the waste glass and the frequency of high scattering zones scales with the Re.Wo. percentage, it is conspicuous that these compounds crystallized from the waste glass during firing. This conclusion is supported by the fact that Fe, Ca and Mg are the essential constituents of Re.Wo. itself. The thermal behaviour of pristine Re.Wo., investigated by HSM and reported in Figure S4 (supplementary materials), further confirmed that the waste glass devitrifies upon heating treatment with a crystallization plateau between 850 and 1180 °C approximately, followed by melting. In addition, the coarse pores in the high scattering zones are compatible with a crystallization process, known in literature as induced crystallization porosity [58–61]. Indeed, the volume variation related to the crystallization induced the formation of spherical intragranular pores in the glassy matrix. This is a peculiar phenomenon of the sinter-crystallization process governing the densification of the glass-ceramics, for which the volume variation accompanying the crystalline phase formation can yield to a shrinkage when the effective viscosity of the bulk is low, or to the formation of additional closed porosity when the viscosity of the system is high [58–61]. In our case, at this low temperature the effective viscosity is quite high (6.5–7.0 log Pa·s, Table S4, supplementary materials).

The partial crystallization of glasses during the sintering of porcelain stoneware is documented in the literature, related to both devitrification of the glass itself and/or to glass-ceramic matrix interactions [31]. Different new-formed phases were detected in minor quantity, depending on the glass type introduced in the ceramic body. Those rich in one or more alkali/alkali-earths can lead to the crystallization of plagioclase [16,30,62] and/or feldspars in general [32,33], as well as gehlenite and wollastonite in presence of high CaO [31]. β-spodumene was detected in ceramic bodies containing B-rich frit with Li [63], while cristobalite formation is known in presence of SLS glass [26,30]. Glasses rich in iron, typically obtained from the melting of iron-rich waste, have been largely employed as precursors in the production of glass-ceramics, thanks to their strong crystallization ability upon second warm-up (see the review of Chinnam et al. [64] for a panoramic on this topic). Otherwise, they are much less investigated in the field of porcelain stoneware, for the well-known bloating issue which Fe_2O_3 can induce during the sintering process [65]. Bernando and co-workers [66] made an attempt, using an iron-rich glass obtained from the plasma melting of asbestos containing waste, as secondary raw materials in different kinds of ceramic products, including porcelain stoneware-like material. The

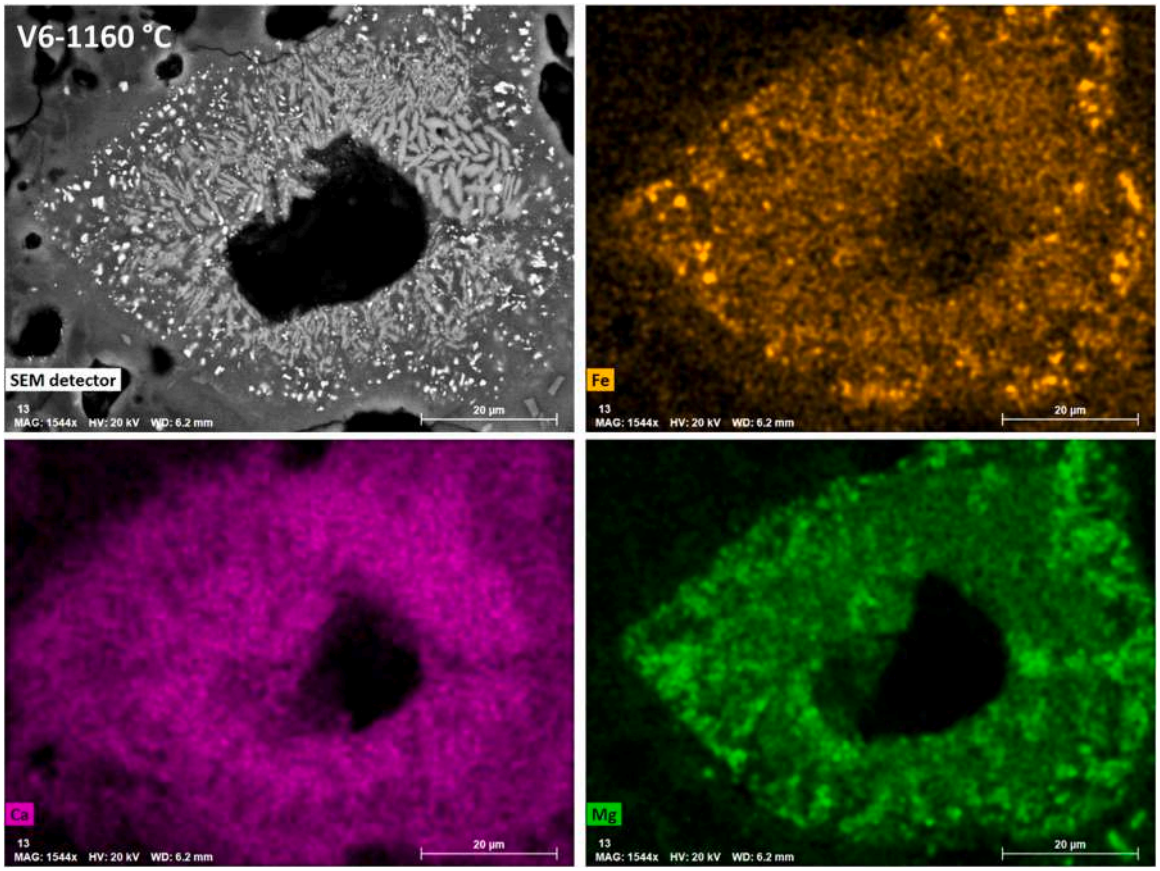

Fig. 6. Elemental distribution maps of sample V6 fired at 1160 °C: detail of the Re.Wo. glass in crystallization. Orange = Fe, Purple = Ca, Green = Mg.

presence of this glassy-waste induced the formation of pyroxene phases, with an intermediate composition among those of augite and diopside, or melilite and anorthite, depending on the heating ramp used for the firing.

In this work, the second phase crystallized from Re.Wo. can be evidenced after HF-etching of the sample surface and secondary electron images (SEI) collected by SEM. By this way, prismatic crystals, grown in parallel aggregates around the coarse pore, are evidenced (Fig. 7). The EDS analyses conducted on these aggregates rendered a composition fully compatible with a pyroxene, such as augite. The identification as augite was confirmed by further micro-Raman and XRPD analyses carried out on the etched samples (Fig. S5a,b, supplementary materials).

Due to augite content below the detection limit of XRPD experiment (mainly for the occurrence of broad peaks with very low signal to noise ratio and partially overlapping major phases), it was not possible to quantify the crystallization ability of Re.Wo., that is, its degree of crystallization upon the second heating treatment [67,68]. It is known that this degree depends on various factors, such as the initial grain size of the glass, the heating ramp (with fast ramps favouring sintering over crystallization), the thermal cycle and the kiln atmosphere [68,69]. Another parameter to take in account is the interaction with the ceramic matrix. In this sense, it appears evident from the elemental distribution (map in Fig. S6, supplementary materials) that, at 1160 °C, the interaction between Re.Wo. and the ceramic matrix is very limited. It can be observed that chemical diffusion is extremely restricted, apart from the *in-situ* crystallization of augite and magnetite, to the point that the glass can be considered a rigid particle with minimal interaction with the surrounding matrix at 1160 °C. This circumstance and the co-presence of MgO and CaO can explain the crystallization of augite rather than anorthite in this system.

3.3.2. Firing at 1180 °C (all batches)

The temperature increase caused a rounding of sharp edges of the particles, along with an increase in the degree of vitrification of the matrix, which, however, still exhibits some porosity (Fig. 8). This porosity appears to be different in the benchmark with respect to the Re.Wo.-bearing batches: still mainly open in V0 (as also testified by the higher water absorption, see [34]), closed in the V3 and especially in the V6-V9 batches, presumably due to crystallization. In this sense, glass crystallization seems to influence the sintering process of the ceramic body by favouring the development of closed spherical pores which will lead, at the T_{md}, to a lower densification efficiency for V6-V9, as observed in the paragraph 3.1. Furthermore, observing the micrographs in detail, it is clear how at 1180 °C the high scattering zones are less sharply defined. This turned the Re.Wo. particles from rigid (with almost no interaction with the matrix) into partially reacted (with diffusion halos of the elements and blurred rim) supporting a certain degree of interaction between Re.Wo. and the surrounding ceramic matrix.

The elemental distribution maps in Fig. 9 actually help to better understand what described above. While at 1160 °C it is possible to clearly distinguish magnetite and augite crystals (Fig. 6), at 1180 °C only the magnetite octahedra are still visible (thanks to high Fe concentration), while augite begins to melt, as evidenced by the diffusion of its components into the surrounding matrix (Fig. 9). The behaviour observed here is consistent with previous studies on an iron-rich glass used as precursor for glass-ceramics [67,68,70]. Indeed, the silica glass obtained by the melting of iron-rich waste underwent crystallization during the heating treatment, firstly of magnetite and then of pyroxene solid solution. These phases are characterized by different stability at high temperature, with magnetite persisting, while pyroxene being affected by a progressive melting as the temperature increases [64,67,68]. SEM images collected on etched samples containing Re.Wo. (Fig. S7, supplementary materials) further confirm the persistence of well-defined magnetite, while augite is scarce and characterized by less defined shapes with respect to the firing at 1160 °C. The elemental distribution maps of V3-V6-V9 at 1180 °C (Fig. S8, supplementary materials) show that the partial dissolution of augite induced a greater interaction with the ceramic matrix, but the diffusion of elements is still limited, as they remain concentrated in the proximity of the Re.Wo. relics.

3.3.3. Firing at 1200 °C (all batches)

Samples V6 and V9 are at their maximum densification temperature, showing a typical compact microstructure with relics of quartz and feldspars crystals (the so-called "skeleton") and rounded isolated pores, dispersed in an abundant vitreous phase (Fig. 10). Pores present a bimodal distribution: a series of small pores (diameter <10 μm) together with relatively large ones (around 20–30 μm in diameter). These latter are probably related to the induced crystallization porosity and cause the slightly lesser efficiency of densification mentioned above. V0 and V3 are still characterized by a significant open porosity, especially the benchmark (5 % and 3 % respectively, compared to 0.6–1 % of V9-V6, see [34]). In all the Re.Wo.-bearing batches, the high scattering zones, corresponding to the waste glass relics, are much less evident than at

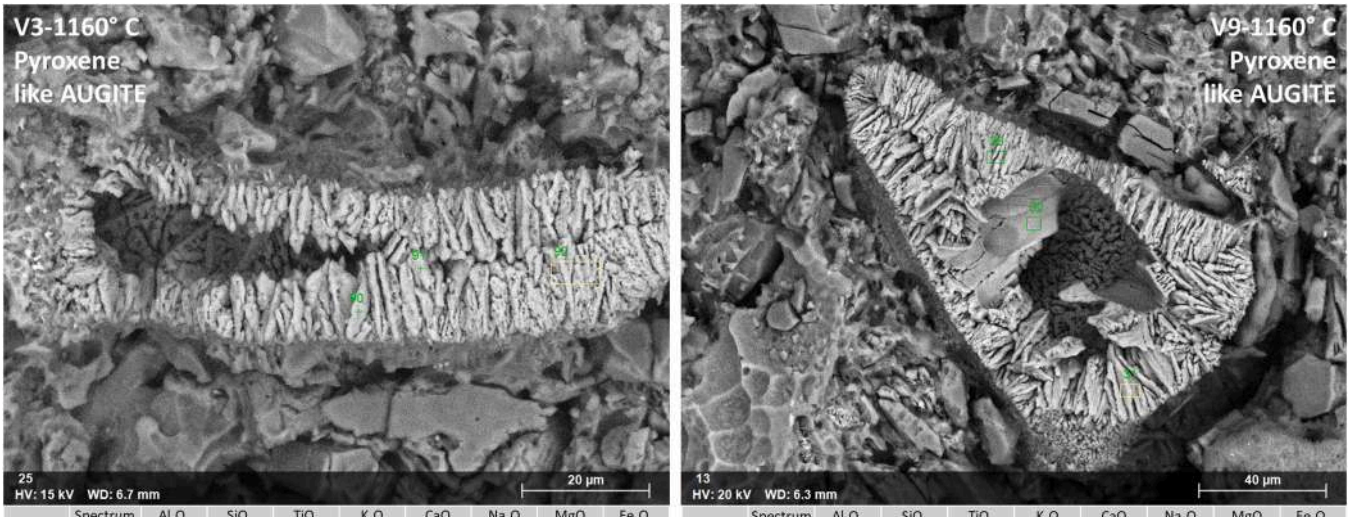

	Spectrum	Al_2O_3	SiO_2	TiO_2	K_2O	CaO	Na_2O	MgO	Fe_2O_3
V3-1160	90	8.66	45.16	1.02	0.05	25.23	0.28	11.45	8.15
V3-1160	91	8.27	47.92	0.82	0.05	22.35	0.35	13.36	6.88
V3-1160	92	10.16	43.90	1.40	0.10	24.02	0.46	11.76	8.21

	Spectrum	Al_2O_3	SiO_2	TiO_2	K_2O	CaO	Na_2O	MgO	Fe_2O_3
V9-1160	29	9.84	46.40	1.20	0.08	25.12	0.63	9.79	6.93
V9-1160	30	5.30	29.15	1.19	0.22	42.37	0.04	8.35	13.37
V9-1160	31	9.50	44.21	0.87	0.00	24.68	0.37	13.28	7.09

Fig. 7. Etched V3 and V9 sample fired at 1160 °C, EDS analyses compatible with a pyroxene phase, such as augite.

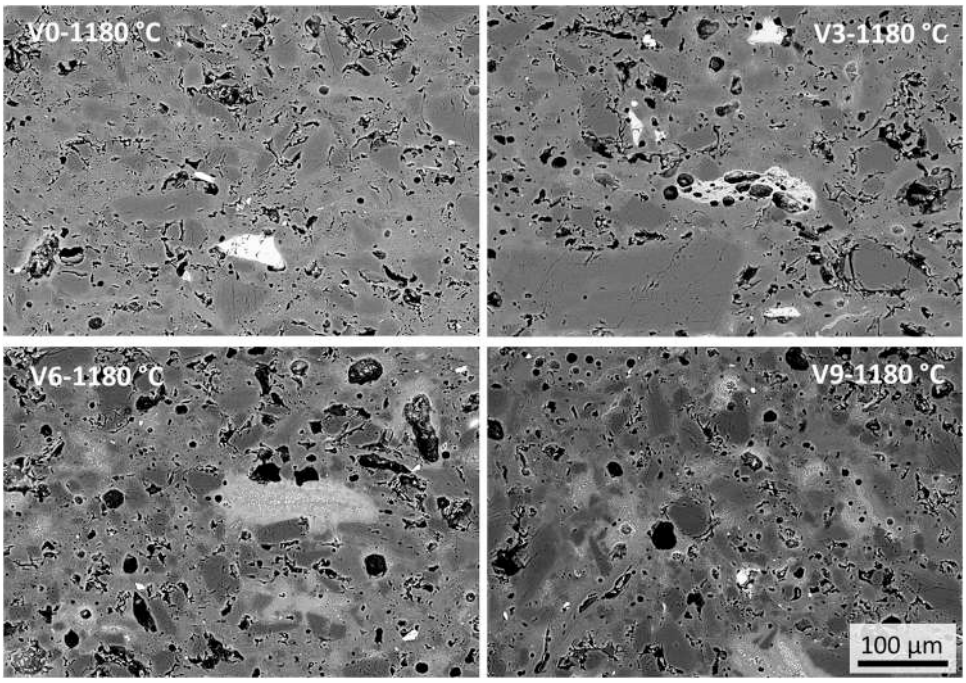

Fig. 8. Backscattering scanning electron microscope image of all samples fired at 1180 °C.

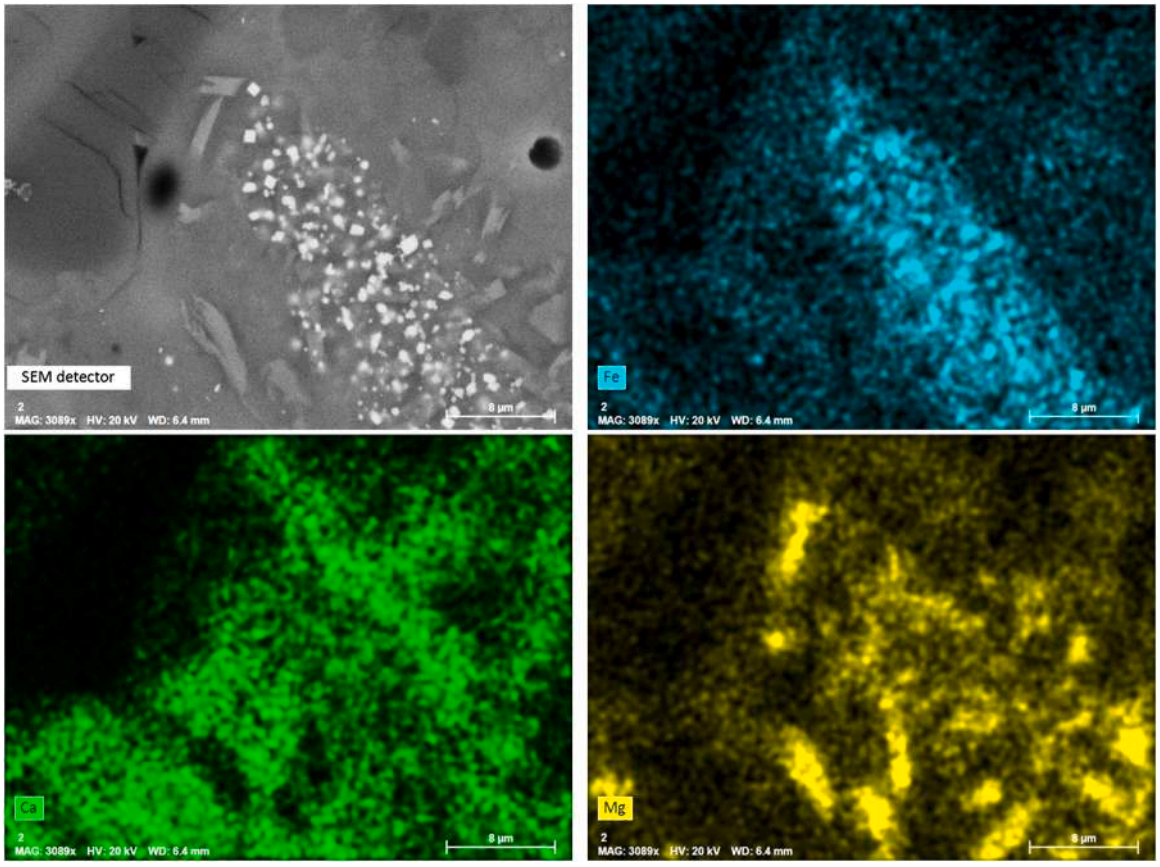

Fig. 9. Elemental distribution maps of sample V9 fired at 1180 °C: detail of the augite melting. Light-blue = Fe; Green = Ca; Yellow = Mg.

lower temperatures, indicating a deeper interaction with the ceramic matrix.

SEM micrographs – collected both at higher magnification (Fig. S9, supplementary materials) and on etched samples (Fig. S10, supplementary materials) – still reveal the presence of magnetite, while augite is no more distinguishable. The elemental distribution maps of V3-V6-V9 at 1200 °C (Fig. S11, supplementary materials) well describe the diffusion of the elements through the matrix, testifying, at this

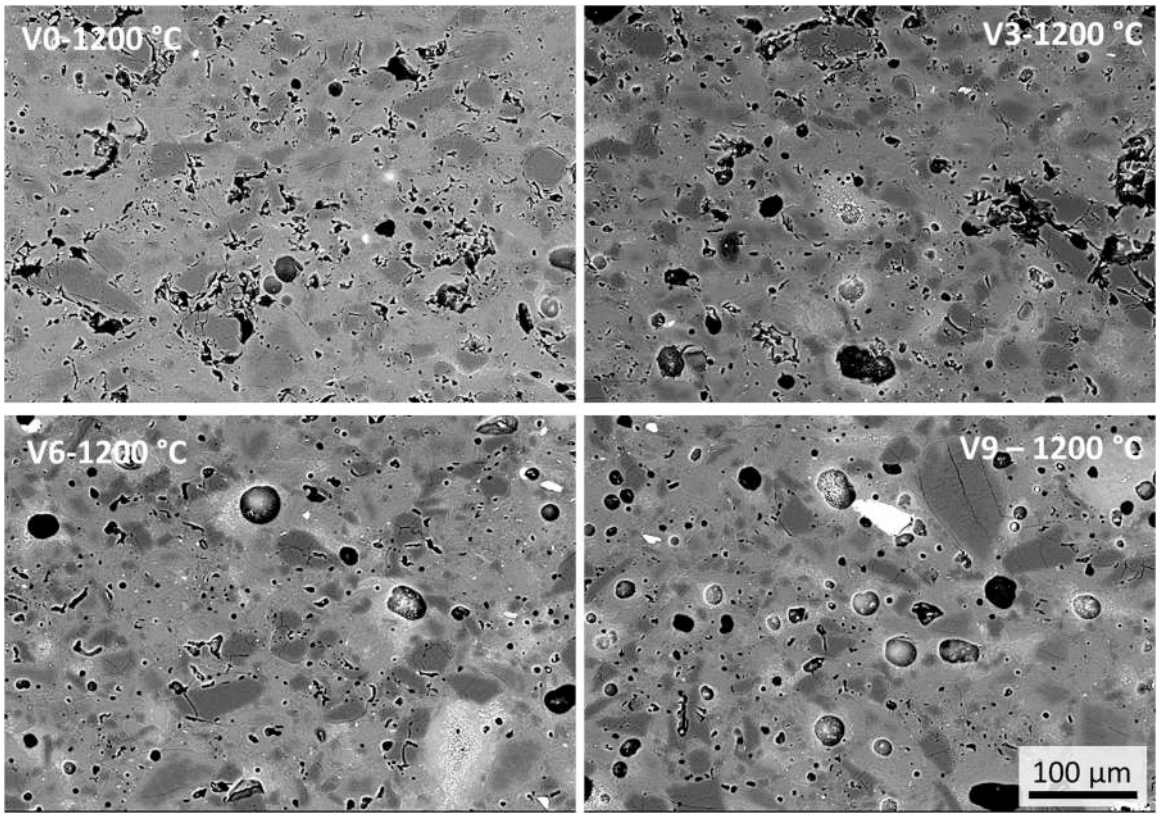

Fig. 10. Backscattering scanning electron microscope image of all samples fired at 1200 °C.

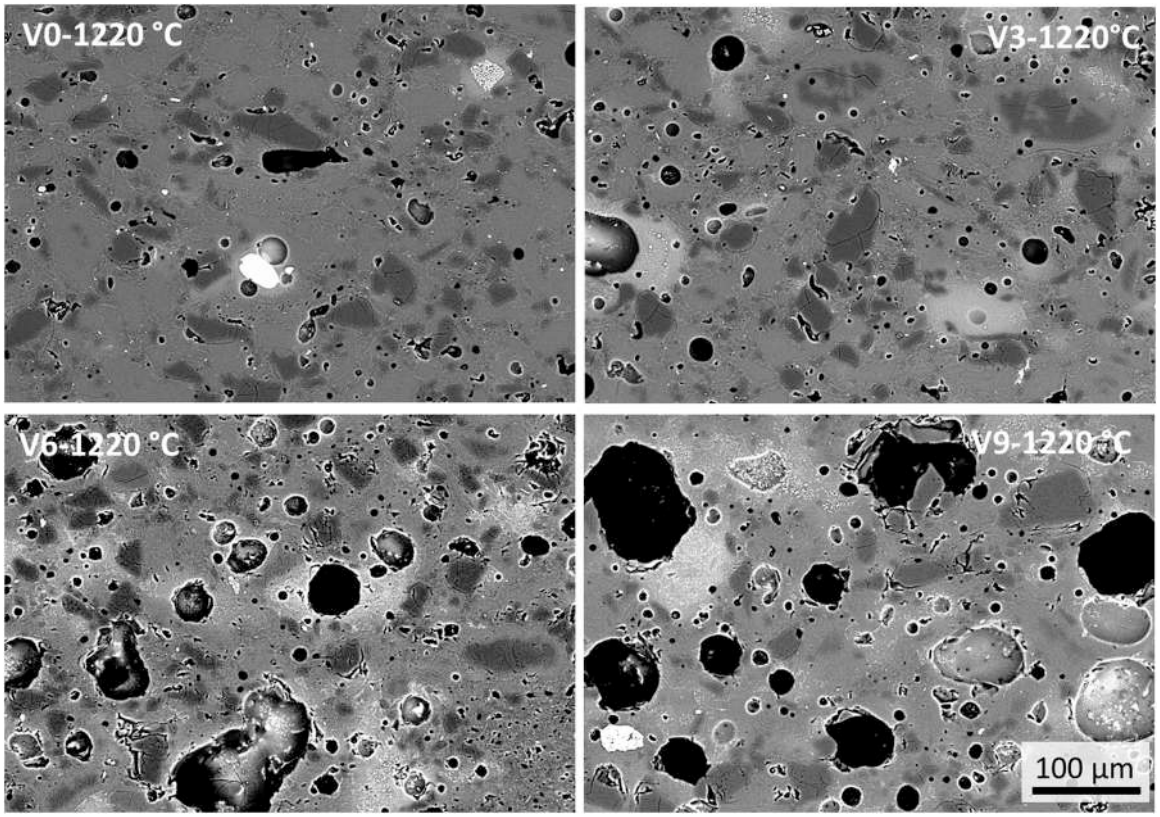

Fig. 11. Backscattering scanning electron microscope image of all samples fired at 1220 °C.

temperature, a significant contribution of Re.Wo. (and the phases crystallized and then melted) to the formation of the amorphous phase, even if not uniformly in the ceramic body.

3.3.4. Firing at 1220 °C (all batches)

V0 and V3 are at their maximum densification temperature and exhibit the typical compact microstructure of porcelain stoneware at this stage of the sintering; on the contrary, V6 and V9 are in evident overfiring conditions (Fig. 11). Such a growth of the pores size with respect to the lower temperature in the two latter samples suggests a strong instability of the ceramic body, related to bloating phenomena. This feature is confirmed by both technological data, with an abrupt loss of bulk density between 1200 and 1220 °C (Table 2), and by HSM data, indicating a very short *plateau* of stability followed by a significant expansion (Table 1). Concerning the high scattering zones, the micrographs reveal that the development of relatively big, closed pores (up to 100 μm in diameter) occurred in correspondence of these areas. This feature may depend on the combination of two phenomena: the porosity induced by crystallization, already described, and the porosity induced by the release of oxygen, stemming from the reduction of Fe^{3+} to Fe^{2+} in overfiring conditions [71,72]. Indeed, a progressive dissolution of magnetite with the increasing temperature (Fig. 4), which implies the release of Fe^{2+} and Fe^{3+} to the melt, was observed. As recently demonstrated by Nodari and co-workers [65] for ceramic bodies with relatively high Fe_2O_3 (~1.5 wt%), the transition between the condition of maximum densification and that of overfiring may shift the $Fe^{3+} \rightleftarrows Fe^{2+}$ equilibrium of the melt towards the reduced species, with oxygen release, boosting bloating phenomena.

SEM images at 1220 °C, collected at higher magnification (Fig. S12, supplementary materials), reveal that nothing remains of Re.Wo. particles, except a halo of diffusion of the elements and some magnetite crystals, as also confirmed by the etched samples (Fig. S13, supplementary materials), where no augite was found.

3.4. Physical properties of the vitreous phase and repercussions on the sintering behaviour of the ceramic bodies

The physical properties of the melt at high temperature were estimated by predictive models based on its chemical composition, as described in the experimental section. Since the quantification of augite was not possible through XRD analysis, its contribution to the melt composition, as consequence of its dissolution, was evaluated based on the SEM results. Actually, the Re.Wo. particles were considered as a single component, including augite. Subtracting the chemical contribution of magnetite (quantified by XRPD) to the total chemistry of the Re.Wo. (Table S3, supplementary materials), we obtained a chemical composition accounting for both crystallized augite and residual glass. Thus, waste glass was treated as a rigid component with a specific chemical composition. As seen above, the SEM-EDS analyses allowed to identify different degrees of interaction between these "particles" and the ceramic matrix at each firing temperature.

At the lowest temperature considered (1160 °C), Re.Wo. was identified as a rigid particle with negligible interaction with the ceramic matrix. Increasing the temperature, a certain degree of interaction, in terms of elements' diffusion, was observed: at first limited to the area immediately surrounding the Re.Wo. relics (at 1180 °C), then increasingly widespread in the ceramic matrix (at 1200–1220 °C). Therefore, we considered every Re.Wo. grain (augite + residual glass) as a 100 % unique rigid particle at 1160 °C (with no contribution to the chemical composition of melt). For the higher temperatures, the amount of Re.Wo. unreacted relics was estimated, based on microstructural images analyses, assuming 50 % (1180 °C), 25 % (1200 °C) and 0 % (1220 °C) of the starting value. This implies a corresponding contribution to the melt chemical composition up to 100 % at 1220 °C. In order to verify the reliability of this hypothesis and carry out cross-interpretations, especially about the stability of the ceramic body, the experimental data of the sintering process (get by HSM) were compared with those calculated

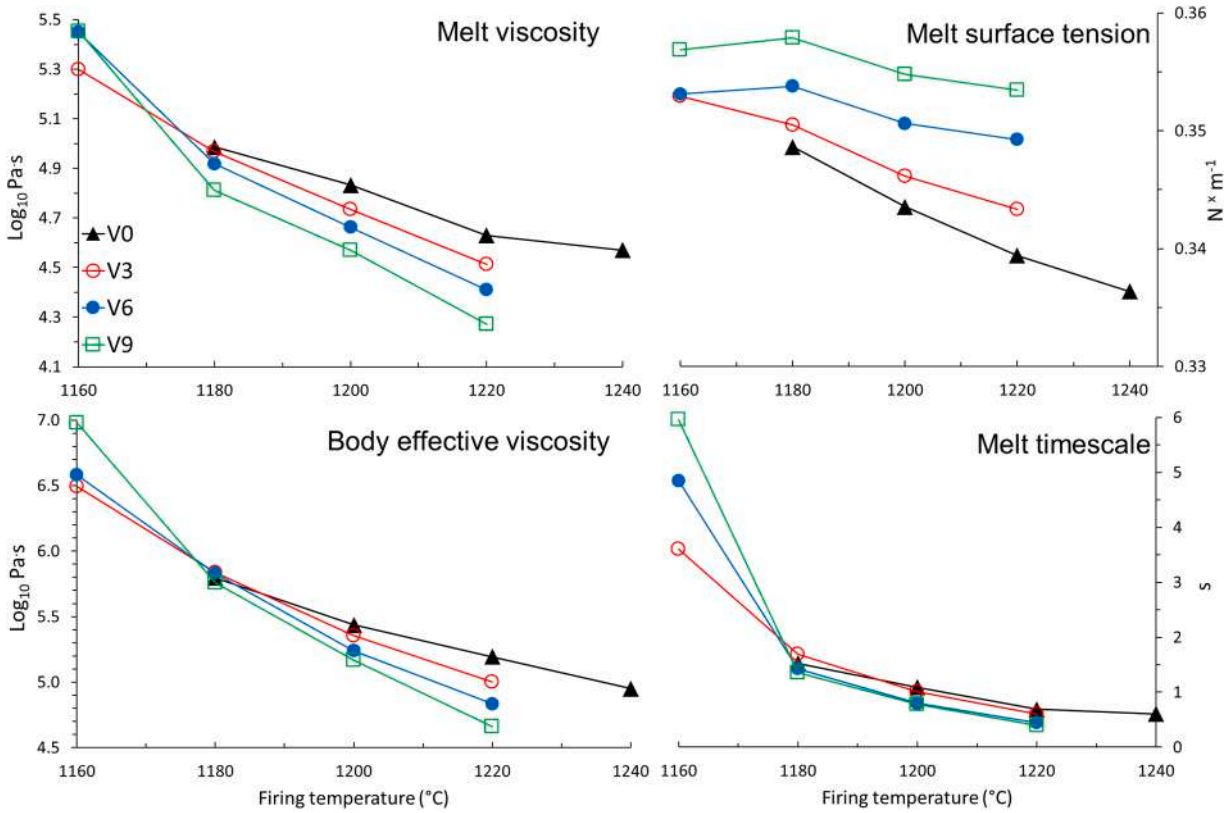

Fig. 12. Trends of calculated shear viscosity (Log_{10} Pa·s), surface tension ($N \cdot m^{-1}$) and timescale (s) of the melt, and effective viscosity of the bulk (Log_{10} Pa·s) as a function of firing temperature (°C). Experimental error is within the symbol size.

from the physical properties of the melt at high temperature (Table S4, supplementary materials).

The predicted physical properties of the melts are reported in Fig. 12, as a function of temperature. It is possible to see that both shear viscosity and surface tension decrease with increasing temperature, but their behaviour is different as a function of Re.Wo. content. Viscosity shows a decrease accompanied by a faster rate from V0 to V9, while the situation is opposite for surface tension, which results to be higher in Re.Wo.-bearing batches, with lower decreasing rates with temperature. This likely reflects the relatively lower silica and higher alkalis and alkali-earths amount of the melts present in Re.Wo.-bearing bodies.

The body effective viscosity accounts for the contribution of the melt viscosity plus the skeleton (or solid load), which, as known, can increase the viscosity of a silicate melt up to several orders of magnitude [73,74]. Here, the effective viscosity decreased with rising temperature: V3, V6 and V9 are characterized by lower values with respect to V0 above 1190 °C (Fig. 12). At temperatures close to maximum densification, such a decrease is proportional to the Re.Wo. addition to the batch. This is the consequence of the natural drop in the viscosity of the melt with increasing temperature, and the simultaneous loss of solid load due to melting of the crystalline components, such as feldspars and, to a lesser extent, quartz.

The timescale describes the sintering kinetics by taking into account the ratio between viscosity and surface tension of the melt, the two key parameters governing the sintering process by viscous flow [35,36,48, 75–79]. Timescale shows that the reaction times of samples with Re.Wo. are slightly faster than those of the benchmark, especially for V6 and V9 starting from 1180 °C onwards (Fig. 12). This is a reflection of the enrichment of Fe, Ca and Mg and of the decrease in silica (due to the significant contribution of the Re.Wo. to the melt chemical composition with increasing temperature). As a consequence, a decrease in viscosity and a simultaneous increase in surface tension of the melts occurred. These results are in good agreement with the kinetics experimentally determined by HSM, which indicate for Re.Wo.-bearing bodies a faster sintering rate with respect to the benchmark (Fig. 3). Indeed, calculated and experimental data appear to be effectively correlated, showing the expected negative relationship between sintering rates and melt timescales for V3-V6-V9 (Fig. 13A). The same relationship can also be perceived for V0, which nevertheless exhibits a very steep sintering rate-timescale trend as a consequence of the smaller variations of the physical properties (especially viscosity) as a function of temperature.

Further interesting cross-interpretations between predicted properties and experimental data can be made in relation to the stability of the ceramic body. As already discussed in the sections on sintering behaviour and microstructure, the bodies with Re.Wo. are characterized by de-sintering phenomena at the maximum temperature tested, showing significant expansion. Nodari et al. [65] recently reported for porcelain stoneware with high iron that: *"the phenomenon of bloating can be attributed to two main causes: i) oxygen release from Fe^{3+} reduction to Fe^{2+} [72] and ii) progressive relaxation until the collapse of the material when the bulk viscosity turns too low* [73]". In this work an iron reduction can be hypothesized for Re.Wo.-bearing bodies at high temperature. This would be related to the magnetite dissolution and to the occurrence of large spheroidal pores, consistent with the release of oxygen due to the reduction of Fe^{3+} at overfiring temperatures, as described in paragraph 3.3. Moreover, the bloating rate is negatively correlated with the effective viscosity in the tested samples, even if in a non-linear way (Fig. 13B). It seems indeed that there is a critical value of effective viscosity of ~5.2–5.3 log Pa·s, below which bloating is triggered. This is in good agreement with previous studies indicating that, in order to ensure an adequate dimensional stability at maximum densification, it is necessary to have an effective viscosity of at least 5.2 log Pa·s [25,26, 36]. Thus, it is likely that the bloating is promoted by the two phenomena acting simultaneously: gas release and excessive decrease of the viscosity of the tile [65].

4. Conclusions

Thermal inertized man-made vitreous fibres MMVF behave differently from other glasses studied in the literature and introduced in porcelain stoneware bodies as fluxing agents. Indeed, there is evidence that Re.Wo. glass is quite refractory and maintains its individuality during firing, behaving as rigid particles during the early stages of sintering and then gradually being incorporated into the melt up to 1220 °C.

The sintering mechanisms, in terms of stages' extent, remain substantially unchanged after addition of Re.Wo., allowing a good densification efficiency of the waste-bearing batches, even if slightly lower than the benchmark. On the other hand, the presence of Re.Wo. affects the densification kinetics, as a result of modest but important variations in microstructure and phase transformations of porcelain stoneware. Actually, Re.Wo. underwent crystallization of two phases (magnetite and augite) during the heating treatment. This crystallization induced the formation of spherical intragranular pores in the glass matrix, as observed by SEM, which slow down the densification process in the early stages, with repercussions also at T_{md}, such as the slightly worsening of densification efficiency. Moreover, augite and magnetite act as buffer of Fe-Ca-Mg, affecting the properties of the ceramic melt increasingly with the rising temperature, when their dissolution induced a diffusion of these elements able to lower the melt viscosity and accelerate the kinetics. The increasing interaction of the Re.Wo. with the ceramic matrix also significantly affected the stability of quartz and

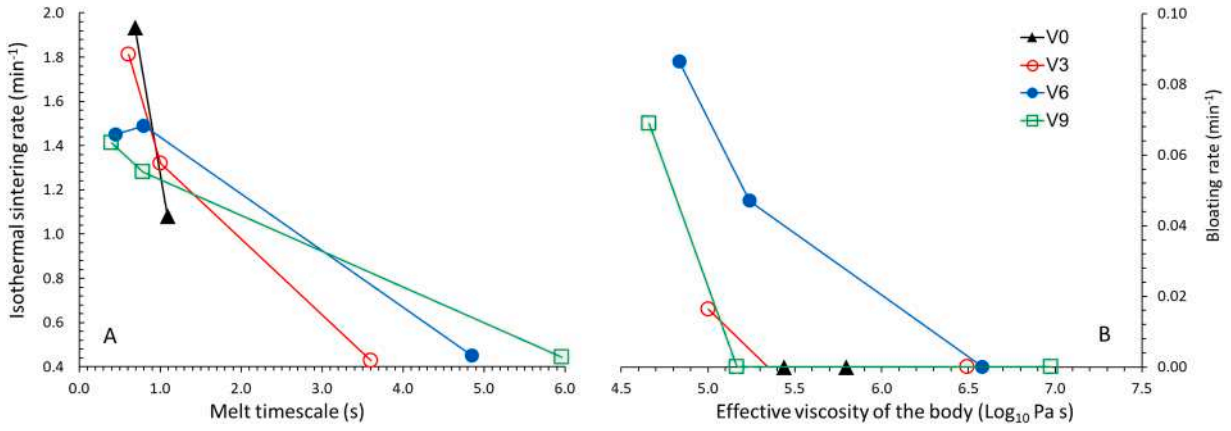

Fig. 13. Trends of isothermal sintering rate (at the constant stage) of porcelain stoneware bodies (experimentally determined by HSM) as a function of melt timescale (calculated) (A); and bloating rate (experimentally determined by HSM) as a function of effective viscosity of the bulk (calculated) (B). Experimental error is within the symbol size.

mullite, implying a decreasing in their amount, while preserving a higher quantity of feldspars and comparable percentage of glassy phase at T_{md}.

The stability at high temperature is comparable for the benchmark and Re.Wo.-bearing bodies at the temperature of maximum densification, while significant development of large closed pores is recorded for the batches with the highest content of waste glass (6–9 wt%) once in overfiring conditions. These bloating phenomena can be attributed to two different causes acting simultaneously: excessive loss of bulk viscosity (due to melting of crystalline phases and decrease in melt viscosity as reflection of enrichment in alkalis and alkali-earths) and release of oxygen (by reduction of $Fe^{3+}$to Fe^{2+}).

This study demonstrated that the glass derived from the thermal inertization of man-made vitreous fibres is easier to incorporate into porcelain stoneware than other peralkaline glasses. This is because its tendency to crystallization allows to not release some fluxing elements to the melt, limiting the interaction with the ceramic matrix at lower temperatures and avoiding an excessive change in the firing behaviour of the body. By this way, classic issues related to the introduction of glass - such as the too strong lowering of the temperature at which the densification starts and the shortening of the decreasing stage, which lead to a lower sintering efficiency - are prevented.

CRediT authorship contribution statement

Zanelli Chiara: Writing – review & editing. **Dondi Michele:** Writing – review & editing, Supervision, Methodology. **Molinari Chiara:** Writing – review & editing, Data curation. **Arletti Rossella:** Writing – review & editing, Validation, Supervision, Project administration, Funding acquisition. **Fantini Riccardo:** Methodology, Investigation, Formal analysis. **Conte Sonia:** Writing – review & editing, Writing – original draft, Visualization, Methodology, Investigation, Formal analysis, Data curation, Conceptualization. **Gualtieri Alessandro F.:** Writing – review & editing, Validation, Project administration, Funding acquisition.

Declaration of Competing Interest

The authors declare that they have no known competing financial interests or personal relationships that could have appeared to influence the work reported in this paper.

Acknowledgements

The paper financed by “From Waste to Resource: Exhausted Man-made Vitreous Fibers Valorization for Green Ceramic Production” (CUP E93C22000800007)” Fondo di Ateneo per la Ricerca 2022 - Linea FOMO UNIMORE and by project “Fibre Vetrose per ceramici green” financed by Ministero dell’Ambiente e della Sicurezza Energetica2022 CUP E93C23002050006. Alessandro F. Gualtieri and Rossella Arletti thanks Project 101113855 – LIFE22-ENV-IT-LIFE ReWo cofunded by the European Union. Riccardo Fantini and Sonia Conte thanks the Project ECOSISTER (ECS_00000033) under the National Recovery and Resilience Plan (NRRP), Mission 04 Component 2 Investment 1.5—Next Generation EU.

Appendix A. Supporting information

Supplementary data associated with this article can be found in the online version at doi:10.1016/j.jeurceramsoc.2025.117230.

References

[1] M. Coronado, T. Blanco, N. Quijorna, R. Alonso-Santurde, A. Andrés, Types of waste, properties and durability of toxic waste-based fired masonry bricks, Eco-Efficient Masonry Bricks and Blocks. Woodhead Publishing (2015) 129–188.
[2] M. Coronado, A.M. Segadães, A. Andrés, Using mixture design of experiments to assess the environmental impact of clay-based structural ceramics containing foundry wastes, J. Hazard. Mater. 299 (2015) 529–539.
[3] E. Cifrian, M. Coronado, N. Quijorna, R. Alonso-Santurde, A. Andrés, Waelz slag-based construction ceramics: effect of the trial scale on technological and environmental properties, J. Mater. Cycles Waste Manag. 21 (6) (2019) 1437–1448.
[4] C. Zanelli, S. Conte, C. Molinari, R. Soldati, M. Dondi, Waste recycling in ceramic tiles: a technological outlook, Resour., Conserv Recycl 168 (2021) 105289.
[5] M. Ardit, C. Zanelli, S. Conte, C. Molinari, G. Cruciani, M. Dondi, Ceramisation of hazardous elements: benefits and pitfalls of the inertisation through silicate ceramics, J. Hazard Mater. 423 (2022) 126851.
[6] M. Dondi, Feldspathic fluxes for ceramics: sources, production trends and technological value, Resour. Conserv Recycl. 133 (2018) 191–205.
[7] L. Baraldi, World production and consumption of ceramic tiles, Ceram. World Rev. 153 (2023) 58–73.
[8] R.V. Silva, J. de Brito, C.Q. Lye, R.K. Dhir, The role of glass waste in the production of ceramic-based products and other applications: a review, J. Clean. Prod. 167 (2017) 346–364.
[9] F. Matteucci, M. Dondi, G. Guarini, Effect of soda-lime glass on sintering and technological properties of porcelain stoneware tiles, Ceram. Int. 28 (8) (2002) 873–880.
[10] C. Carbonchi, P. Danasino, R. Lorici, R. Riveriti, E. Castelli, Impiego di fondenti additivati con vetro in un impasto da gres porcellanato, Ceram. Inf. 426 (2003) 580–587.
[11] E. Rambaldi, A. Tucci, L. Esposito, Glass recycling in porcelain stoneware tiles: firing behaviour, Ceram. Forum Int. cfi-Ber. DKG 81 (3) (2004) E32–E36.
[12] E. Rambaldi, W.M. Carty, A. Tucci, L. Esposito, Using waste glass as a partial flux substitution and pyroplastic deformation of a porcelain stoneware tile body, Ceram. Int. 33 (5) (2007) 727–733.
[13] A. Tucci, L. Esposito, E. Rastelli, C. Palmonari, E. Rambaldi, Use of soda-lime scrap-glass as a fluxing agent in a porcelain stoneware tile mix, J. Eur. Ceram. Soc. 24 (1) (2004) 83–92.
[14] A. Tucci, E. Rambaldi, L. Esposito, Use of scrap glass as raw material for porcelain stoneware tiles, Adv. Appl. Ceram. 105 (1) (2006) 40–45.
[15] I.M. Bakr, Effect of waste glass and zircon on ceramic properties and microstructure of porcelain tiles, Adv. Appl. Ceram. 104 (5) (2005) 243–248.
[16] Y. Pontikes, A. Christogerou, G.N. Angelopoulos, E. Rambaldi, L. Esposito, A. Tucci, Use of scrap soda–lime–silica glass in traditional ceramics, Glass Technol. 46 (2) (2005) 200–206.
[17] T. Tarvornpanich, G.P. Souza, W.E. Lee, Microstructural evolution on firing soda–lime–silica glass fluxed whitewares, J. Am. Ceram. Soc. 88 (5) (2005) 1302–1308.
[18] A.P. Luz, S. Ribeiro, Use of glass waste as a raw material in porcelain stoneware tile mixtures, Ceram. Int. 33 (5) (2007) 761–765.
[19] G. Viruthagiri, R. Gobi, B. Rajamannan, Mechanical properties related to use of glass waste as a raw material in porcelain stoneware tile mixtures, Recent Res. Sci. Technol. 1 (2) (2009) 52–57.
[20] D. Fraga, A. Gyozova, S. Kozhukharov, S. Allepuz, C. Lázaro, V. Trilles, J. Carda, Development of new ecological ceramic tiles by recycling of waste glass and ceramic materials, Sci. Univ. Rousse 50 (2011) 8–11.
[21] S. Mustafi, M. Ahsan, A.H. Dewan, S. Ahmed, N. Khatun, N. Absar, Effect of waste glass powder on physico-mechanical properties of ceramic tiles, Bangladesh J. Sci. Res. 24 (2) (2012) 169–180.
[22] K.O. Ajanaku, M. Pal, S.K. Das, Differences in vitrification behaviour of flint and opaque scrap glass containing porcelainized stoneware body, Ceram. Forum Int. cfi/Ber. DKG 92 (3) (2015) 31–34.
[23] S. Chitwaree, J. Tiansuwan, N. Thavarungkul, L. Punsukumtana, Energy saving in sintering of porcelain stoneware tile manufacturing by using recycled glass and pottery stone as substitute materials, Case Stud. Therm. Eng. 11 (2018) 81–88.
[24] N. Marinoni, D. D’Alessio, V. Diella, A. Pavese, F. Francescon, Effects of soda–lime–silica waste glass on mullite formation kinetics and microstructures development in vitreous ceramics, J. Environ. Manag. 124 (2013) 100–107.
[25] S. Conte, C. Zanelli, C. Molinari, G. Guarini, M. Dondi, Glassy wastes as feldspar substitutes in porcelain stoneware tiles: thermal behaviour and effect on sintering process, Mater. Chem. Phys. 256 (2020) 123613.
[26] S. Conte, C. Molinari, M. Ardit, G. Cruciani, M. Dondi, C. Zanelli, Porcelain versus porcelain stoneware: so close, so different. sintering kinetics, phase evolution, and vitrification paths, Materials 16 (1) (2023) 171.
[27] M. Raimondo, C. Zanelli, F. Matteucci, G. Guarini, M. Dondi, J.A. Labrincha, Effect of waste glass (TV/PC cathodic tube and screen) on technological properties and sintering behaviour of porcelain stoneware tiles, Ceram. Int. 33 (4) (2007) 615–623.
[28] N.M.F. Andreola, L. Barbieri, E. Karamanova, I. Lancellotti, M. Pelino, Recycling of CRT panel glass as fluxing agent in the porcelain stoneware tile production, Ceram. Int. 34 (5) (2008) 1289–1295.
[29] K. Kim, K. Kim, J. Hwang, Characterization of ceramic tiles containing LCD waste glass, Ceram. Int. 42 (6) (2016) 7626–7631.
[30] M. Lassinantti Gualtieri, C. Mugoni, S. Guandalini, A. Cattini, D. Mazzini, C. Alboni, C. Siligardi, Glass recycling in the production of low-temperature stoneware tiles, J. Clean. Prod. 197 (2018) 1531–1539.
[31] E. Bernardo, A. Dattoli, E. Bonomo, L. Esposito, E. Rambaldi, A. Tucci, Application of an industrial waste glass in “glass–ceramic stoneware”, Int. J. Appl. Ceram. Technol. 8 (5) (2011) 1153–1162.
[32] E. Bernardo, L. Esposito, E. Rambaldi, A. Tucci, S. Hreglich, Recycle of waste glass into “glass–ceramic stoneware”, J. Am. Ceram. Soc. 91 (7) (2008) 2156–2162.

[33] E. Bernardo, L. Esposito, S. Hreglich, E. Rambaldi, G. Timellini, A. Tucci, Tailored waste based glasses as secondary raw materials for porcelain stoneware, Adv. Appl. Ceram. 107 (6) (2008) 322–328.
[34] R. Arletti, S. Conte, C. Zanelli, M. De Iuliis, D. Di Giuseppe, V. Scognamiglio, D. Malferrari, M. Dondi, A.F. Gualtieri, Recycling the product of thermal inertization of man-made vitreous fibres for the manufacture of stoneware tiles, Waste Biomass Valoriz. 14 (2023) 1721–1736, https://doi.org/10.1007/s12649-022-01959-8.
[35] S. Conte, C. Zanelli, M. Ardit, G. Cruciani, M. Dondi, Phase evolution during reactive sintering by viscous flow: disclosing the inner workings in porcelain stoneware firing, J. Eur. Ceram. Soc. 40 (2020) 1738–1752.
[36] S. Conte, C. Zanelli, M. Ardit, G. Cruciani, M. Dondi, Predicting viscosity and surface tension at high temperature of porcelain stoneware bodies: a methodological approach, Materials 11 (2018) 2475.
[37] T. Degen, M. Sadki, E. Bron, U. König, G. Nénert, The HighScore suite, Powder Diffr. 29 (2014), https://doi.org/10.1017/S0885715614000840.
[38] A. Gualtieri, Accuracy of XRPD QPA using the combined Rietveld–RIR method, J. Appl. Crystallogr. 33 (2000), https://doi.org/10.1107/S002188989901643X.
[39] A.F. Gualtieri, G.D. Gatta, R. Arletti, G. Artioli, P. Ballirano, G. Cruciani, A. Guagliardi, D. Malferrari, N. Masciocchi, P. Scardi, Quantitative phase analysis using the Rietveld method: towards a procedure for checking the reliability and quality of the results, Period. di Mineral. 88 (2019), https://doi.org/10.2451/2019PM870.
[40] N. Doebelin, R. Kleeberg, Profex: a graphical user interface for the Rietveld refinement program BGMN, J. Appl. Crystallogr. 48 (2015) 1573–1580, https://doi.org/10.1107/S1600576715014685.
[41] D. Giordano, J.K. Russell, D.B. Dingwell, Viscosity of magmatic liquids: a model, Earth Planet. Sci. Lett. 271 (1-4) (2008) 123–134.
[42] A.A. Appen, Chemistry of Glass, Khimiya, Saint Petersburg, Russia, 1974, p. 351.
[43] A. Dietzel, Relation between the surface tension and the structure of molten glass, Kolloid Z. 100 (1942) 368–380.
[44] J. Vasseur, F.B. Wadsworth, Y. Lavallee, K.U. Hess, D.B. Dingwell, Volcanic sintering: timescales of viscous densificationand strength recovery, Geophys. Res. Lett. 40 (2013) 5658–5664.
[45] A. Costa, L. Caricchi, N. Bagdassarov, A model for the rheology of particle-bearing suspensions and partially molten rocks, Geochem. Geophys. 10 (2009) 1–13.
[46] C.T. Brasileiro, S. Conte, F. Contartesi, F.G. Melchiades, C. Zanelli, M. Dondi, A. O. Boschi, Effect of strong mineral fluxes on sintering of porcelain stoneware tiles, J. Eur. Ceram. Soc. 41 (11) (2021) 5755–5767.
[47] C.J. McConville, A. Shah, W.M. Carty, Quartz dissolution into porcelain glasses, Ceram. Eng. Sci. Proc. 25 (2) (2004) 51–57.
[48] J.L. Amorós, E. Blasco, A. Moreno, C. Feliu, Kinetics of the transformations occurring during the firing process of an industrial spray-dried porcelain stoneware body, Ceram. Int. 48 (12) (2022) 17611–17620.
[49] Gómez-Tena, M.P., Gilabert, J., Zumaquero, E., Díaz-Canales, E.M., Arrufat, S., Domínguez, R. (2024). Reactivity of crystalline silica in processing ceramic tiles, in: Proceedings of the Eighteenth World Congress on Ceramic Tile Quality, QUALICER2024, Castellón (Spain), 5-6 March, 14.
[50] C. Molinari, S. Conte, M. Dondi, C. Zanelli, Content of crystalline silica phases in porcelain stoneware, Open Ceram. 19 (2024) 100650, https://doi.org/10.1016/j.oceram.2024.100650.
[51] S. Conte, D. Buonamico, T. Magni, R. Arletti, M. Dondi, G. Guarini, C. Zanelli, Recycling of bottom ash from biomass combustion in porcelain stoneware tiles: effects on technological properties, phase evolution and microstructure, J. Eur. Ceram. Soc. 42 (2022) 5153–5163.
[52] S. Conte, C. Molinari, M. Ardit, L. Mantovani, M. Tribaudino, G. Cruciani, M. Dondi, C. Zanelli, Hazardous element inertisation in vitrified silicate ceramics: effect of different matrices, J. Hazard. Mater. 474 (2024) 134657.
[53] Conte, S., Molinari, C., Ardit, M., Cruciani, G., Giordano, D., Dondi, M., Zanelli, C. (in preparation). Vitrification Paths in Porcelain Stoneware: Dependence on Bulk Chemical Composition and Effect on Sintering Behaviour.
[54] A.F. Gualtieri, Thermal behavior of the raw materials forming porcelain stoneware mixtures by combined optical and in situ x-ray dilatometry, J. Am. Ceram. Soc. 90 (4) (2007) 1222–1231.
[55] Carty, W.M. (2003). Glass phase composition in porcelains and correlation with pyroplastic deformation, Whitewares and Materials: Ceramic Engineering and Science Proceedings 24108–132.
[56] T.T. Mbakop, J.G.N. Deutou, L. Boubakar, N. Billong, U.C. Melo, E. Kamseu, V. M. Sglavo, Enhancing the crystallization phenomena and strength of porcelain stoneware: the role of CaO, J. Therm. Anal. Calorim. 144 (2021) 91–106.
[57] K. Traore, T.S. Kabre, P. Blanchart, Gehlenite and anorthite crystallisation from kaolinite and calcite mix, Ceram. Int. 29 (4) (2003) 377–383.
[58] A. Karamanov, M. Pelino, Sinter-crystallisation in the diopside–albite system Part I. Formation of induced crystallisation porosity, J. Eur. Ceram. Soc. 26 (2006) 2511–2517.
[59] A. Karamanov, M. Pelino, Sinter-crystallisation in the diopside–albite system Part II. Kinetics of crystallization and sintering, J. Eur. Ceram. Soc. 26 (2006) 2519–2526.
[60] A. Karamanov, M. Pelino, Induced crystallization porosity and properties of sintereds diopside and wollastonite glass-ceramics, J. Eur. Ceram. Soc. 28 (2008) 555–562.
[61] V.M. Fokin, A.S. Abyzov, J.W.P. Schmelzer, E.D. Zanotto, Stress induced pore formation and phase selection in a crystallizing stretched glass, J. Non Cryst. Solids 356 (2010) 1679–1688.
[62] M.L. Ligabue, A.F. Gualtieri, M. Lassinantti Gualtieri, D. Malferrari, G. Lusvardi, Recycling of thermally treated cement-asbestos for the production of porcelain stoneware slabs, J. Clean. Prod. 247 (2020) 119084.
[63] A.F. Gualtieri, Development of Low-Firing B-Fluxed Stoneware Tiles, J. Am. Ceram. Soc. 92 (11) (2009) 2571–2577 (2009).
[64] R.K. Chinnam, A.A. Francis, J. Will, E. Bernardo, A.R. Boccaccini, Review. Functional glasses and glass-ceramics derived from iron rich waste and combination of industrial residues, J. Non Cryst. Solids 365 (2013) 63–74.
[65] L. Nodari, S. Conte, L. Casini, M. Sisti, R. Fantini, A.F. Gualtieri, C. Molinari, C. Zanelli, D. Giordano, M. Dondi, R. Arletti, Role of iron-rich clays on sintering of porcelain stoneware tiles, J. Eur. Ceram. Soc. 45 (2) (2025) 116947, https://doi.org/10.1016/j.jeurceramsoc.2024.116947.
[66] E. Bernardo, L. Esposito, E. Rambaldi, A. Tucci, Sintered glass ceramic articles from plasma vitrified asbestos containing waste, Adv. Appl. Ceram. 110 (6) (2011).
[67] A. Karamanov, C. Cantalini, M. Pelino, A. Hreglich, Kinetics of Phase Formation in Jarosite Glass-ceramic, J. Eur. Ceram. Soc. 19 (1999) 527–533.
[68] A. Karamanov, G. Taglieri, M. Pelino, Iron-rich sintered glass-ceramics from industrial wastes, J. Am. Ceram. Soc. 82 (11) (1999) 3012–3016.
[69] M.O. Prado, E.D. Zanotto, Glass sintering with concurrent crystallization, C. R. Chim. 5 (2002) 773–786.
[70] A. Karamanov, Vitrification and sinter-crystallization of iron-rich industrial wastes, ISSN: 1662-0356, Adv. Sci. Technol. 92 (2014) 174–183, https://doi.org/10.4028/www.scientific.net/AST.92.174.
[71] F. Sandrolini, C. Palmonari, Role of iron oxides in the bloating of vitrified ceramic materials, Trans. J. Br. Ceram. Soc. 75 (1976) 25–32.
[72] V.C. Kress, I.S. Carmichael, Stoichiometry of the iron oxidation reaction in silicate melts, Am. Mineral. 73 (11-12) (1988) 1267–1274.
[73] D. Giordano, Advances in the rheology of natural multiphase silicate melts: importance for magma transport and lava flow emplacement, Ann. Geophys. 61 (2019) 1–6.
[74] A. Costa, Viscosity of high crystal content melts: dependence on solid fraction, Geophys. Res. Lett. 32 (2005) L22308.
[75] F. Cambier, A. Leriche, Vitrification, in: R.W. Cahn, P. Hanson, E.J. Kramer (Eds.), Processing of Ceramics Part II 17B (VCH Basel) (1996) 124–144.
[76] M.O. Prado, E.D. Zanotto, R. Müller, Model for sintering polydispersed glass particles, J. Non Cryst. Solids 279 (2001) 169–178.
[77] Salem, S., Salem, A. (2013). Mechanisms of momentum transport in viscous flow sintering. INTECH Open Access Publisher.
[78] F.B. Wadsworth, J. Vasseur, E.W. Llewellin, D.B. Dingwell, Hot sintering of melts, glasses and magmas, Rev. Mineral. Geochem. 87 (2022) 801–840.
[79] S. Conte, C. Molinari, M. Dondi, G. Guarini, C. Zanelli, Effect of milling and compaction on sintering of porcelain stoneware tiles, Ceram. Int. 50 (14) (2024) 25228–25240, https://doi.org/10.1016/j.ceramint.2024.04.253.

SUPPLEMENTARY MATERIALS

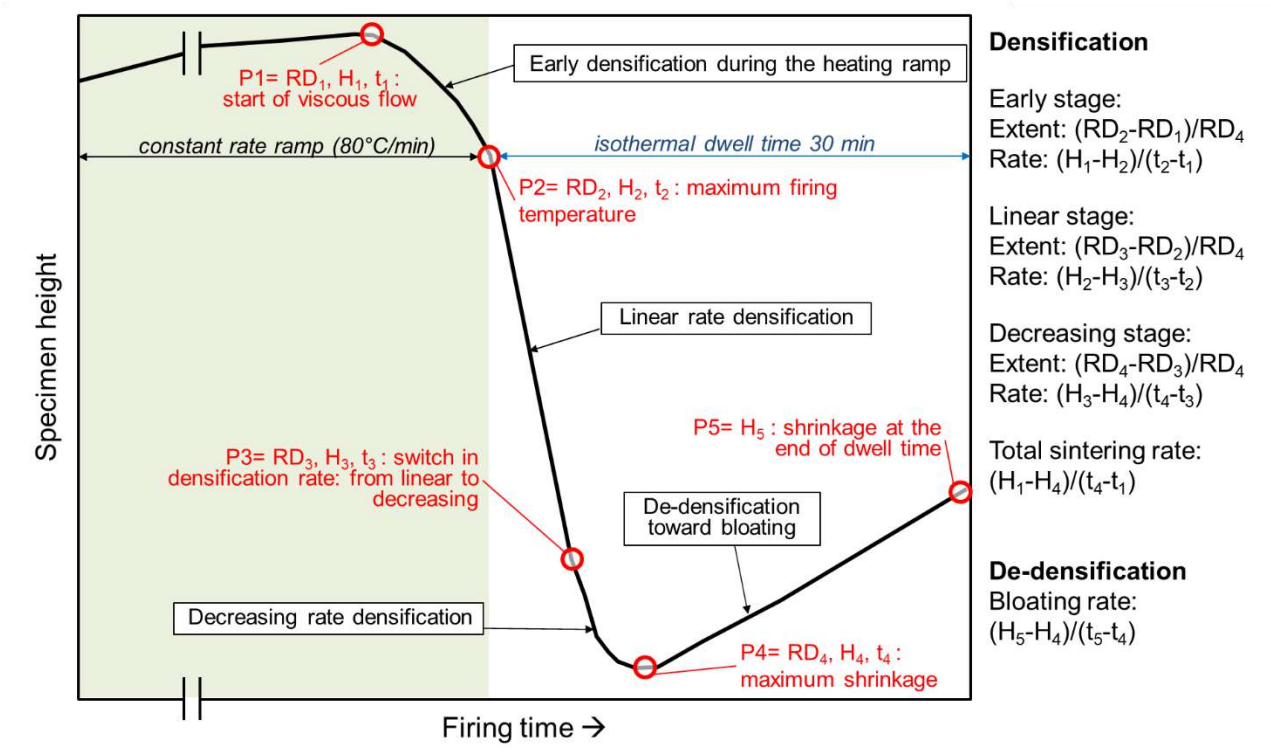

Figure S1. The curve describes the linear shrinkage as a function of firing time during the isothermal run. Different stages of sintering are pointed out, with the relative turning points. Since the mechanisms governing the viscous flow sintering are known, it is possible to describe the process through the parameterization of the firing curve. At temperatures around 1000 °C, a viscous mass transport begins with a given shrinkage (from P1 to P2). This early densification occurs during the heating ramp and is promoted by the flow of the neo-formed liquid phase. Once the sample reaches the maximum firing temperature, the sintering enters the isothermal stage (from P2 to P4), with a first linear rate (from P2 to P3) and then a decreasing rate (the final densification from P3 to P4). Once reached the maximum density, an inversion of the sintering process may take place, leading to a more or less accentuated expansion, with a bloating quantified from P4 to P5. (RD = relative density, calculated by the starting density (bulk density/specific weight of powders) and the volumetric shrinkage during firing, H = height of the specimen and t = time at the point PX, with X: 1-5).

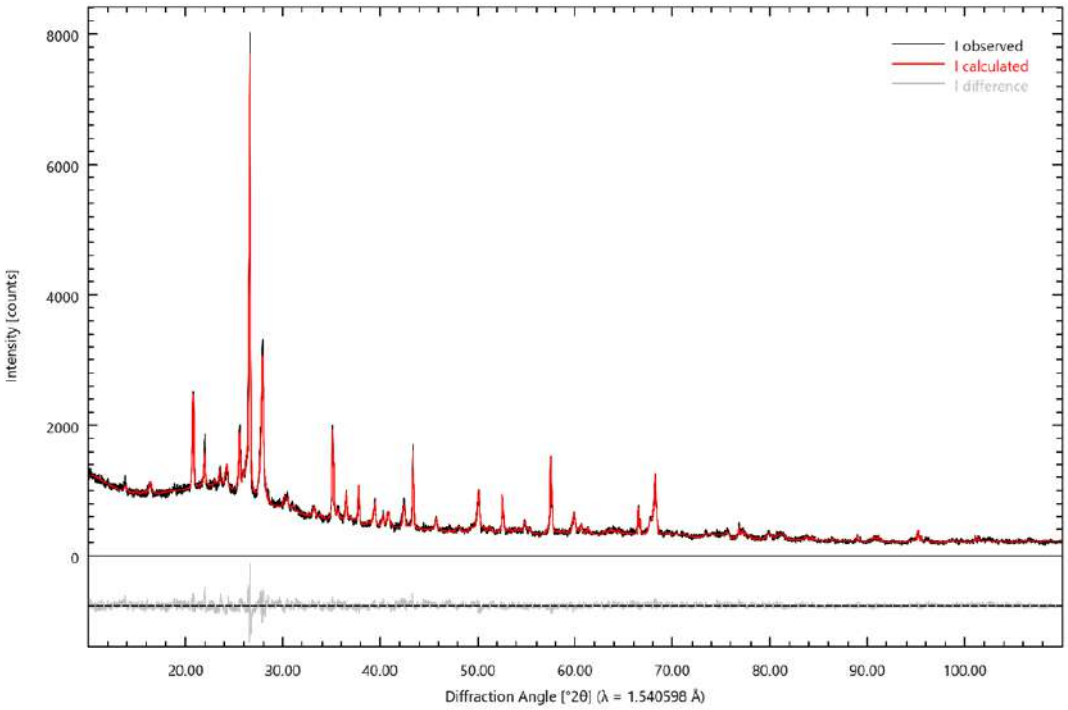

Figure S2. Graphical results of Rietveld refinement for sample V9 fired at 1200 °C.

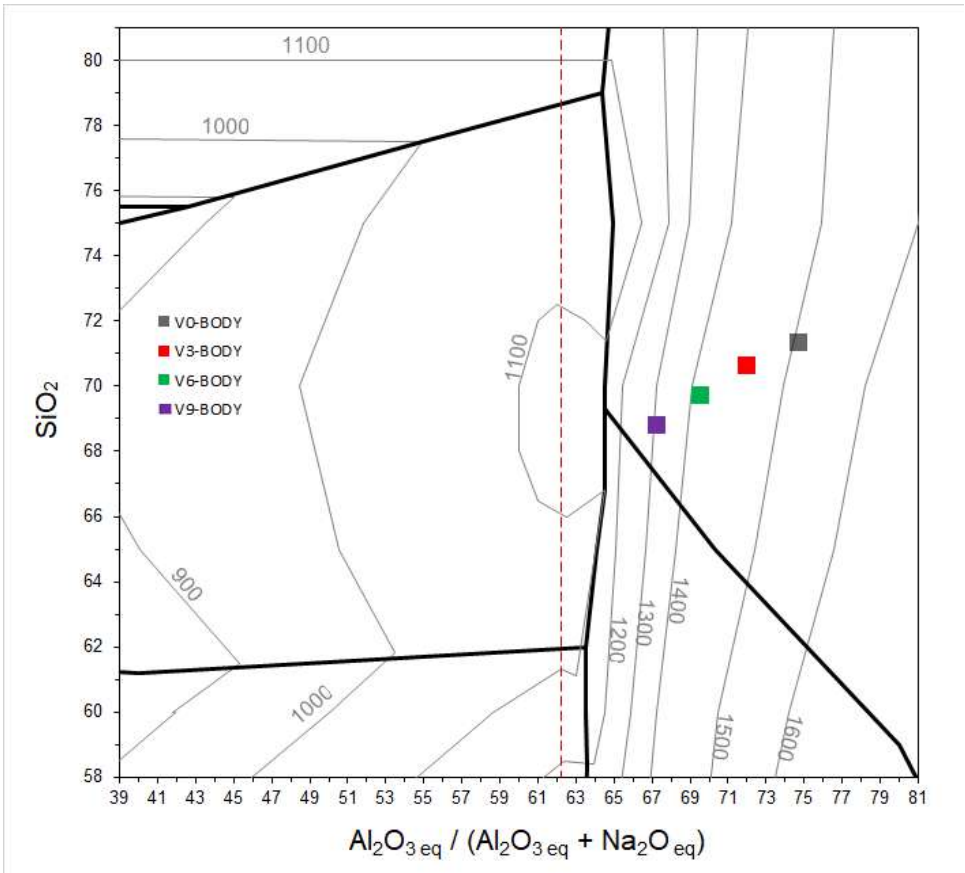

Figure S3. Alumosity-silica diagram with batch compositions. For the diagram construction, see Conte et al. [25].

Figure S4. The thermal behaviour of Re.Wo., investigate by HSM (Misura 3-402ES/3, Expert System Solution) with a cycle of 10 °C/min up to 1600 °C. Crystallization *plateau* between 850 and 1180 °C approximately, followed by melting.

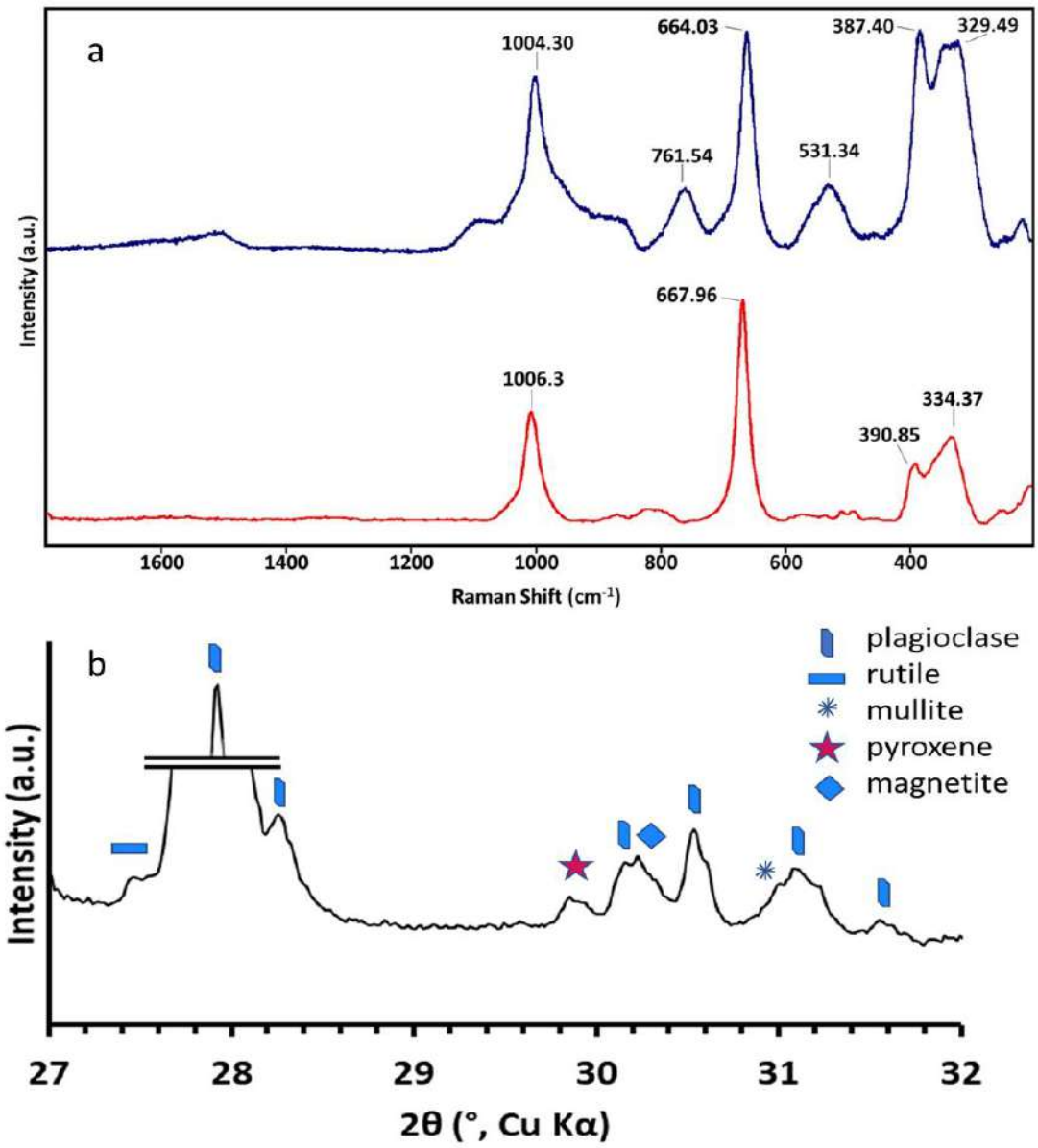

Figure S5. a) Micro-Raman on the etched V9 sample fired at 1180 °C: Augite ref (Red), blue V9-1180-4 30”x3acc, 50X laser green. b) XRPD measurement with long exposure time on the etched V9-1160 °C sample; for augite the shown peak represents the most intense line.

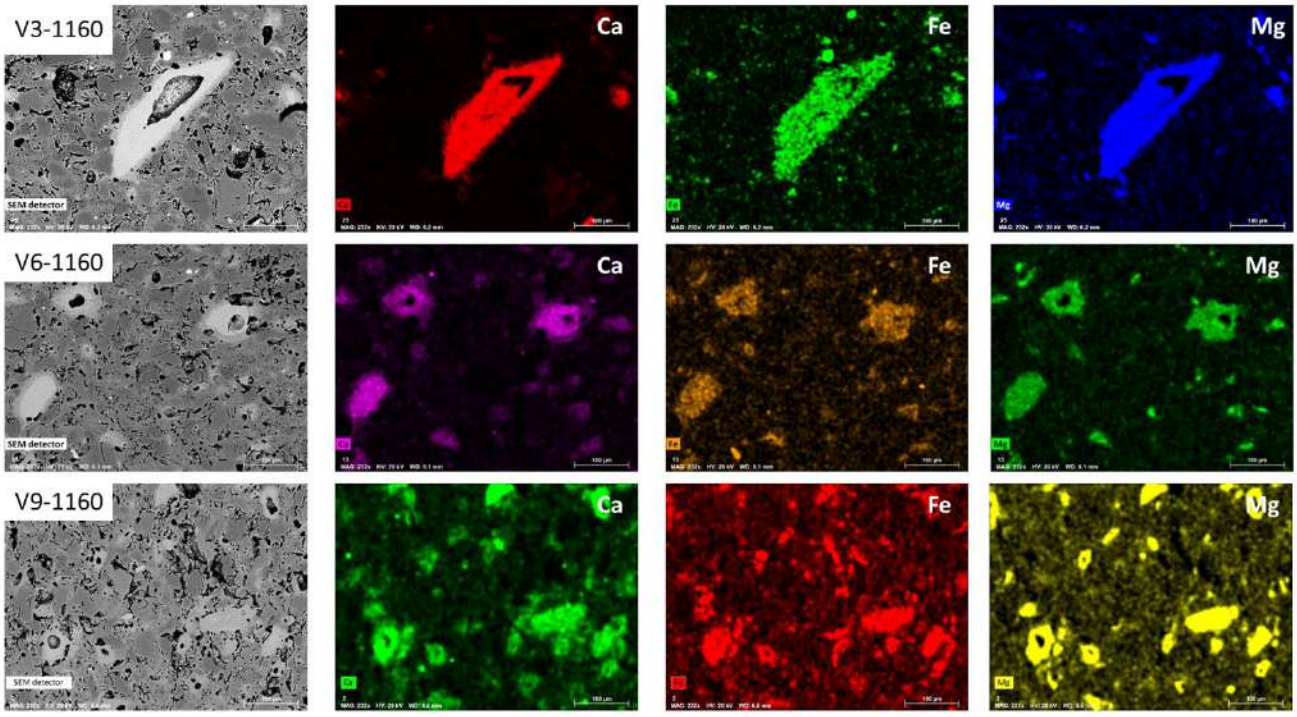

Figure S6. Elemental distribution maps of V3-V6-V9 samples at 1160 °C: Re.Wo. glass crystallization. *In-situ* crystallization of augite and magnetite, no interaction with the ceramic matrix.

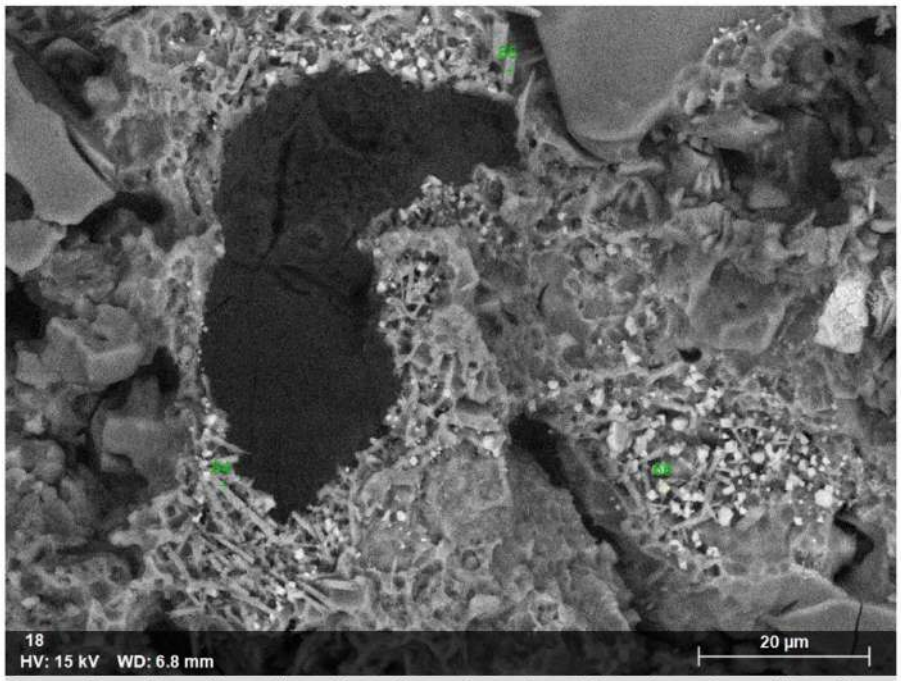

Spectrum	O	Na	Mg	Al	Si	P	K	Ca	Ti	Cr	Fe	Ni	Zr
64	62.11	1.42	8.84	6.25	17.45	0.02	0.22	1.20	0.32	0.00	2.04	0.06	0.08
65	59.75	0.39	15.43	3.16	18.81	0.01	0.02	0.43	0.12	0.00	1.79	0.02	0.05
66	14.28	0.57	5.44	5.46	5.34	0.09	0.19	0.81	1.11	1.02	65.15	0.46	0.09

Figure S7. Etched V3 sample fired at 1180 °C: magnetite octahedra are clearly visible, while augite is less present.

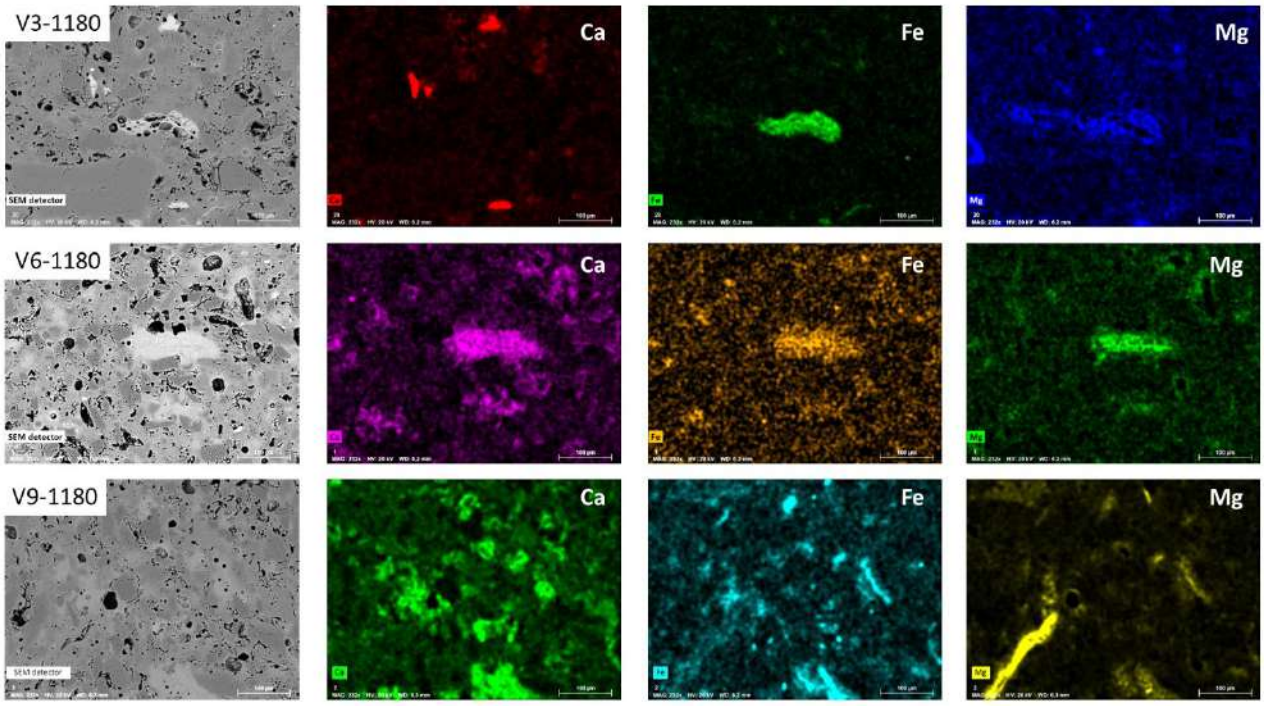

Figure S8. Elemental distribution maps of V3-V6-V9 samples at 1180 °C: partial dissolution of augite induced a greater interaction with the ceramic matrix, but the diffusion of elements is still limited, concentrated in the proximity of the *Re.Wo.* relics.

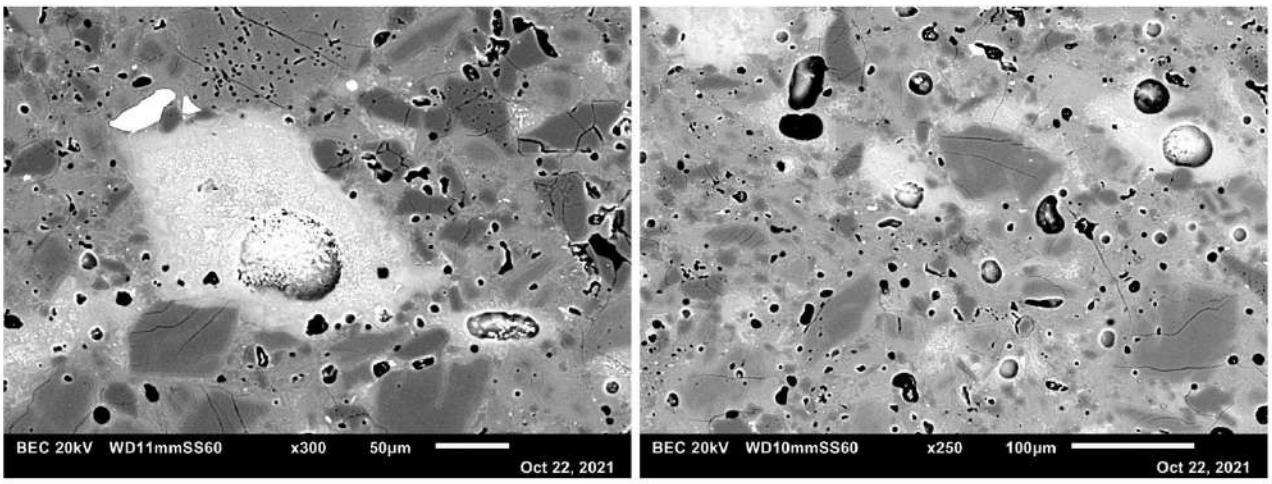

Figure S9. Backscattering scanning electron microscope image of V6 sample fired at 1200 °C: presence of distinguishable magnetite, augite no more distinguishable

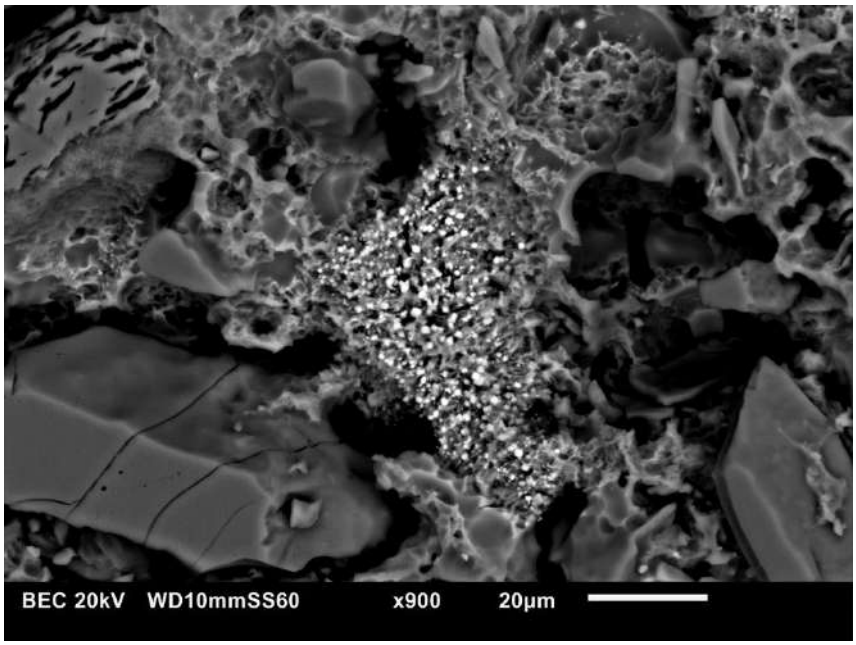

Figure S10. Etched V9 sample fired at 1200 °C: distinguishable magnetite, augite no more distinguishable

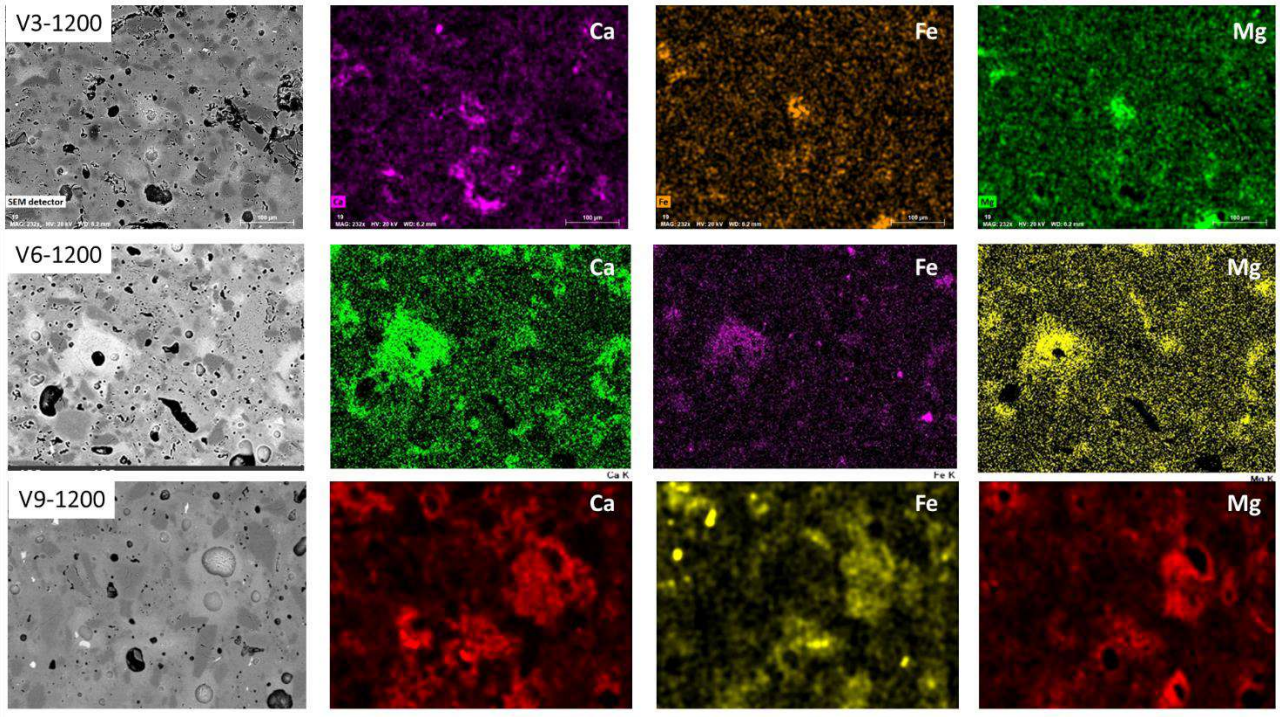

Figure S11. The elemental distribution maps of V3-V6-V9 at 1200 °C: diffusion of the elements through the matrix, significant contribution of *Re.Wo.* (and the phases crystallized and then melted) to the formation of the amorphous phase, even if not uniformly in the ceramic body.

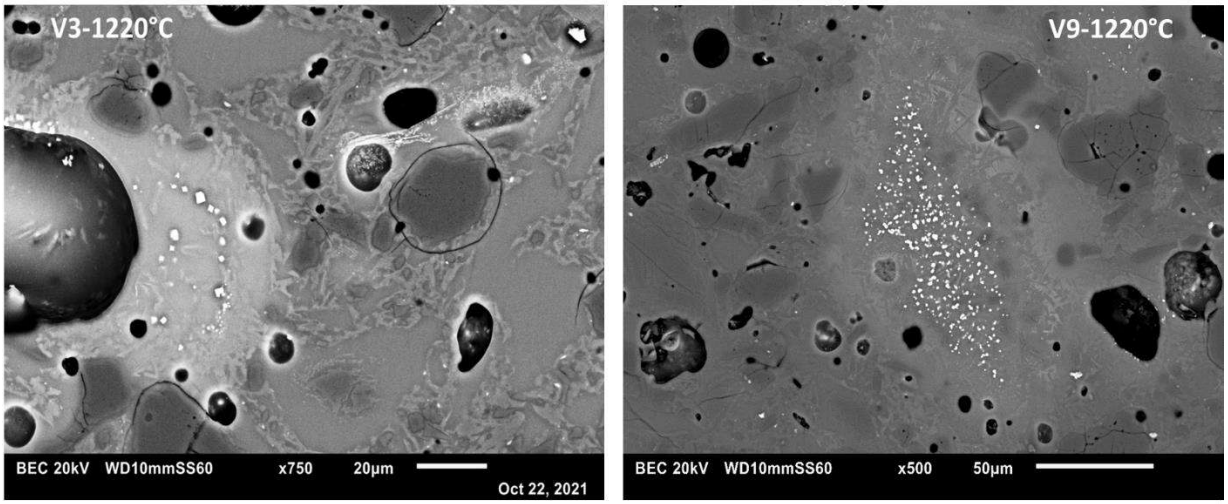

Figure S12. Backscattering scanning electron microscope image of V3 and V9 samples fired at 1220 °C, remains of *Re.Wo.* particles: element diffusion halo and magnetite crystals.

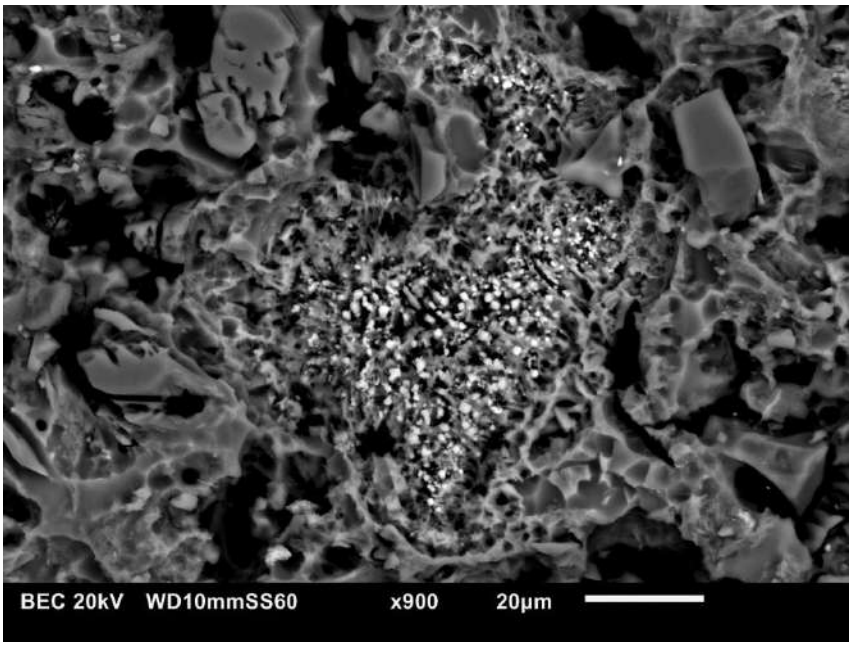

Figure S13. Etched V9 sample fired at 1220 °C: magnetite crystals, no augite found.

Table S1. Formulations of the batches and their chemical composition (wt%) calculated considering the contribution by weight of each raw material.

wt%		**V0**	**V3**	**V6**	**V9**
PLASTIC COMPONENT	**Ball Clay**	35	35	35	35
	Kaolin	5	5	5	5
FLUXES	**Sodic feldspar**	45	42	39	36
FILLER	**Quartz-feldspar sand**	3	3	3	3
	Silica sand	12	12	12	12
RECYCLED material	***Re.Wo.***	0	3	6	9
SiO_2		68.01	67.21	66.41	65.62
Al_2O_3		19.94	19.81	19.68	19.54
TiO_2		0.62	0.65	0.67	0.70
Fe_2O_3		0.44	0.69	0.94	1.19
CaO		0.53	1.10	1.68	2.25
MgO		0.57	0.89	1.21	1.52
K_2O		1.27	1.28	1.29	1.29
Na_2O		4.54	4.29	4.05	3.80
P_2O_5		0.09	0.09	0.09	0.08
MnO		0.00	0.01	0.02	0.03
LOI		4.00	3.99	3.98	3.97
Totale		100	100	100	100

Table S2. Results and details of refinements of the quantitative phase analyses.

	V0				V3				V6				V9			
	V0-1180	**V0-1200**	**V0-1220**	**V0-1240**	**V3-1160**	**V3-1180**	**V3-1200**	**V3-1220**	**V6-1160**	**V6-1180**	**V6-1200**	**V6-1220**	**V9-1160**	**V9-1180**	**V9-1200**	**V9-1220**
	wt.%	wt.%	wt.%	wt.%	wt.%	wt.%	wt.%	wt.%	wt.%	wt.%	wt.%	wt.%	wt.%	wt.%	wt.%	wt.%
	1180	1200	1220	1240	1160	1180	1200	1220	1160	1180	1200	1220	1160	1180	1200	1220
quartz*	22.9	21.6	21.9	18.2	22.9	21.6	20.5	20.0	20.5	20.5	18.8	17.4	21.6	19.5	16.8	16.0
mullite*	8.9	9.1	9.9	8.7	9.0	8.8	9.1	9.2	8.3	8.3	7.8	6.9	8.3	7.7	6.8	5.9
plagioclase*	14.5	7.9	5.0	0.7	21.6	16.2	9.0	4.1	20.9	17.5	9.4	5.7	23.6	18.7	12.3	6.1
rutile*	0.2	0.1	0.2	0.1	0.1	0.2	0.1	0.1	0.1	0.1	0.1	0.0	0.1	0.3	0.2	0.0
magnetite*/**	-	-	-	-	0.2	0.2	0.1	0.1	0.3	0.3	0.3	0.1	0.7	0.6	0.5	0.3
amorphous phase	53.5	61.2	63.0	72.3	46.1	52.9	61.2	66.4	50.0	53.3	63.7	69.8	45.7	53.2	63.5	71.7
Goodness-of-fit statistics* **																
R_p (%)	4.5	4.5	4.4	4.2	4.7	4.2	4.4	4.3	4.7	4.6	4.5	5.2	6.5	4.6	4.6	5.3
R_{wp}(%)	5.7	5.7	5.7	5.5	6.1	5.5	5.6	5.5	6.0	5.9	5.8	6.4	8.5	5.8	5.8	6.7
CHI2**	1.6	1.6	1.6	1.6	1.8	1.5	1.5	1.5	1.7	1.7	1.7	2.2	1.6	1.6	1.8	2.5
σ																
quartz	0.3	0.2	0.2	0.2	0.3	0.3	0.2	0.3	0.3	0.3	0.2	0.2	0.5	0.3	0.3	0.2
mullite	0.1	0.2	0.2	0.2	0.2	0.1	0.2	0.2	0.2	0.2	0.2	0.1	0.4	0.2	0.2	0.2
plagioclase	0.2	0.2	0.2	0.1	0.3	0.2	0.2	0.2	0.3	0.3	0.2	0.1	0.5	0.3	0.3	0.2
rutile	0.1	0.0	0.0	0.0	0.1	0.1	0.0	0.0	0.1	0.1	0.0	0.0	0.1	0.1	0.0	0.0
magnetite	-	-	-	-	0.1	0.1	0.0	0.0	0.1	0.1	0.0	0.0	0.1	0.1	0.0	0.0
amorphous phase	0.4	0.3	0.4	0.3	0.5	0.4	0.4	0.4	0.4	0.4	0.4	0.2	0.8	0.5	0.5	0.3

* The crystal structures employed for the Rietveld refinements are from the following references:

- quartz: Glinnemann, J., King Jr, H. E., Schulz, H., Hahn, T., La Placa, S. J., & Dacol, F. (1992). Crystal structures of the low-temperature quartz-type phases of SiO_2 and GeO_2 at elevated pressure. Zeitschrift für Kristallographie-Crystalline Materials, 198(1-4), 177-212 https://doi.org/10.1524/zkri.1992.198.14.177);
- mullite: Angel, R. J., & Prewitt, C. T. (1986). Crystal structure of mullite: a re-examination of the average structure. American Mineralogist, 71(11-12), 1476-1482;
- plagioclase: Meneghinello, E., Alberti, A., & Cruciani, G. (1999). Order-disorder process in the tetrahedral sites of albite. American Mineralogist, 84(7-8), 1144-1151 https://doi.org/10.2138/am-1999-7-817)
- rutile: Baur, W. H. (1956). Über die verfeinerung der kristallstrukturbestimmung einiger vertreter des rutiltyps: TiO_2, SnO_2, GeO_2 und MgF_2. Acta Crystallographica, 9(6), 515-520 https://doi.org/10.1107/S0365110X56001388);

- magnetite: Wechsler, B. A., Lindsley, D. H., & Prewitt, C. T. (1984). Crystal structure and cation distribution in titanomagnetites (Fe_3-$xTixO_4$). American Mineralogist, 69(7-8), 754-770);
- standard corundum used for amorphous phase quantification: Ishizawa N, Miyata T, Minato I, Marumo F, Iwai S. A structural investigation of alpha-Al_2O_3 at 2170 K. Acta Crystallographica. B36 (1980) 228-230.

** Magnetite contents are close to quantification limit (See e.g.: Giacobbe, C., Gualtieri, A. F., Quartieri, S., Rinaudo, C., Allegrina, M., & Andreozzi, G. B. (2010). Spectroscopic study of the product of thermal transformation of chrysotile-asbestos containing materials (ACM). European Journal of Mineralogy, 22(4), 535-546. https://doi.org/10.1127/0935-1221/2010/0022-2038; Gualtieri, A. F., Viani, A., Sgarbi, G., & Lusvardi, G. (2012). In vitro biodurability of the product of thermal transformation of cement–asbestos. Journal of hazardous materials, 205, 63-71. https://doi.org/10.1016/j.jhazmat.2011.12.005; Viani, A., Gualtieri, A. F., Pollastri, S., Rinaudo, C., Croce, A., & Urso, G. (2013). Crystal chemistry of the high temperature product of transformation of cement-asbestos. Journal of Hazardous Materials, 248, 69-80. https://doi.org/10.1016/j.jhazmat.2012.12.030).

*** Goodness-of-fit statistics are from Bergmann, J., Friedel, P., Kleeberg, R. (1998). IUCr Commission on Powder Diffraction Newsletter, No. 20, 5-8.

Table S3. Chemical composition of Re.Wo. determinate by WD-XRF. For analytical details see Arletti et al., 2023.

	SiO2	TiO2	Al2O3	Fe2O3	MnO	MgO	CaO	Na2O	K2O	P2O5
Re.Wo.	43.66	1.18	13.45	8.52	0.31	10.78	19.89	1.57	0.57	0.07

Table S4. Chemical composition and physical properties at high temperature of the amorphous phase and the bulk body

		V0	V0	V0	V0	V3	V3	V3	V3	V6	V6	V6	V6	V9	V9	V9	V9
Optimal firing temperature	°C	1180	1200	1220	1240	1160	1180	1200	1220	1160	1180	1200	1220	1160	1180	1200	1220
SiO_2	wt.%	67.01	67.98	68.47	69.32	66.63	66.92	67.56	67.63	67.45	66.00	66.58	66.17	66.21	65.87	66.17	65.20
TiO_2	wt.%	0.78	0.81	0.72	0.74	1.18	0.94	0.85	0.81	1.29	1.26	0.95	0.95	1.50	0.79	0.76	0.96
Al_2O_3	wt.%	21.10	20.23	19.60	19.47	21.37	20.66	19.79	19.49	21.28	20.88	20.33	20.35	22.41	21.15	20.54	20.60
Fe_2O_3	wt.%	0.85	0.74	0.72	0.63	0.66	0.82	0.92	0.94	0.46	0.92	0.93	1.22	0.00	0.67	0.96	1.35
MgO	wt.%	1.10	0.96	0.94	0.82	1.43	1.50	1.40	1.39	1.45	1.97	1.77	1.80	1.83	2.31	2.22	2.22
CaO	wt.%	1.03	0.90	0.87	0.76	1.36	1.68	1.66	1.73	1.38	2.44	2.35	2.50	1.81	3.07	3.13	3.27
Na_2O	wt.%	5.65	6.21	6.57	6.43	4.32	4.92	5.62	6.00	3.75	3.78	4.96	5.08	2.77	3.44	4.04	4.53
K_2O	wt.%	2.48	2.17	2.11	1.84	3.04	2.57	2.20	2.01	2.95	2.75	2.14	1.92	3.47	2.70	2.18	1.88
Melt surface tension	$N \cdot m^{-1}$	0.349	0.344	0.339	0.336	0.353	0.351	0.346	0.343	0.353	0.355	0.351	0.349	0.357	0.358	0.355	0.353
Melt shear viscosity (in log unit)	Pa·s	4.99	4.83	4.63	4.57	5.30	4.97	4.74	4.51	5.45	4.94	4.66	4.41	5.45	4.81	4.57	4.27
Melt timescale	s	1.53	1.09	0.69	0.61	3.60	1.69	1.00	0.61	4.85	1.49	0.80	0.45	5.96	1.36	0.78	0.40
Bulk solid fraction	1	0.46	0.39	0.37	0.28	0.56	0.48	0.39	0.34	0.55	0.52	0.38	0.30	0.62	0.51	0.38	0.28
Bulk relative viscosity	1	6.46	4.02	3.66	2.40	15.67	7.41	4.17	3.09	13.62	9.61	3.78	2.66	33.51	8.84	3.95	2.46
Bulk effective viscosity (in log unit)	Pa·s	5.80	5.44	5.19	4.95	6.49	5.84	5.36	5.00	6.58	5.92	5.24	4.84	6.98	5.76	5.17	4.66